



1 **Low Cobalt Inventories in the Amundsen and Ross Seas Driven by High Demand for**
2 **Labile Cobalt Uptake Among Native Phytoplankton Communities**

3 **Rebecca J. Chmiel^{1,2}, Riss M. Kellogg^{1,2}, Deepa Rao^{1,2}, Dawn M. Moran², Giacomo R.**
4 **DiTullio³, and Mak A. Saito²**

5 ¹ MIT/WHOI Joint Program in Oceanography/Applied Ocean Science and Engineering, Woods
6 Hole, MA, 02543, USA

7 ² Department of Marine Chemistry and Geochemistry, Woods Hole Oceanographic Institution,
8 Woods Hole, MA, 02543, USA

9 ³ Hollings Marine Laboratory, 331 Fort Johnson, Charleston SC, 29412, USA

10

11 Corresponding author: Mak Saito (msaito@whoi.edu)

12 **Key Points:**

- 13 • A significantly smaller dCo inventory was observed in the Ross Sea during the
14 2017/2018 austral summer compared to two expeditions in 2005/2006.
- 15 • The drawdown of the labile dCo fraction can be explained by higher rates of Co uptake
16 by phytoplankton.
- 17 • This change may be due to the alleviation of Fe limitation through inputs from increased
18 glacial melting and subsequent development of intermittent vitamin B₁₂ and/or Zn
19 limitation, both of which would be expected to increase the demand for Co among
20 plankton communities.



21 Abstract

22 Cobalt (Co) is a scarce but essential micronutrient for marine plankton in the Southern Ocean and
23 coastal Antarctic seas where dissolved cobalt (dCo) concentrations can be extremely low. This
24 study presents total dCo and labile dCo distributions measured via shipboard voltammetry in the
25 Amundsen Sea, Ross Sea and Terra Nova Bay during the CICLOPS (Cobalamin and Iron Co-
26 Limitation of Phytoplankton Species) expedition. A significantly smaller dCo inventory was
27 observed during the 2017/2018 CICLOPS expedition compared to two 2005/2006 expeditions to
28 the Ross Sea conducted over a decade earlier. The dCo inventory loss (~10–20 pM) was present
29 in both the surface and deep ocean and was attributed to the loss of labile dCo, resulting in the
30 near-complete complexation of dCo by strong ligands in the photic zone. A changing dCo
31 inventory in Antarctic coastal seas could be driven by the alleviation of iron (Fe) limitation in
32 coastal areas where the flux of Fe-rich sediments from melting ice shelves and deep sediment
33 resuspension may have shifted the region towards vitamin B₁₂ and/or zinc (Zn) limitation, both of
34 which are likely to increase the demand for Co among marine plankton. High demand for Zn by
35 phytoplankton can result in increased Co and cadmium (Cd) uptake because these metals often
36 share the same metal uptake transporters. This study compared the magnitudes and ratios of Zn,
37 Cd and Co uptake (ρ) across upper ocean profiles and observed order of magnitude uptake trends
38 ($\rho_{\text{Zn}} > \rho_{\text{Cd}} > \rho_{\text{Co}}$) that paralleled the trace metal concentrations in seawater. High rates of Co and
39 Zn uptake were observed throughout the region, and the speciation of available Co and Zn
40 appeared to influence trends in dissolved metal : phosphate stoichiometry and uptake rates over
41 depth. Multi-year loss of the dCo inventory throughout the water column may be explained by an
42 increase in Co uptake into particulate organic matter (POM) and subsequently increased flux of
43 Co into sediments via sinking and burial. This perturbation of the Southern Ocean Co
44 biogeochemical cycle could signal changes in the nutrient limitation regimes, phytoplankton
45 bloom composition, and carbon sequestration sink of the Southern Ocean.

46 Plain Language Summary

47 Cobalt is an important micronutrient for plankton, yet is often scarce throughout the oceans. A
48 2017/2018 expedition to coastal Antarctica, including regions of the Amundsen Sea and the Ross
49 Sea, discovered lower concentrations of cobalt compared to two past expeditions in 2005 and 2006.
50 In particular, this expedition observed lower concentrations of deep-ocean labile cobalt, or “free”
51 cobalt unbound to strong organic molecules, the type of cobalt preferred by phytoplankton for
52 uptake as a micronutrient. It is possible that a shifting nutrient landscape due to changing inputs
53 of other micronutrients like dissolved iron is causing the lower dissolved cobalt concentrations,
54 and may also be affecting the demand for micronutrients like dissolved zinc and vitamin B₁₂, which
55 contains a cobalt atom. We have modeled how increased cobalt uptake by plankton can result in
56 the lower deep cobalt concentrations over a time period of 12 years.

57 1 Introduction

58 Coastal Antarctic seas are highly productive environments for phytoplankton blooms and
59 are characterized by high nutrient, low chlorophyll (HNLC) surface waters that tend to be growth
60 limited by iron (Fe) and other trace metal micronutrients (Martin et al., 1990; Arrigo et al., 2008,
61 2012). During the spring and summer months, katabatic winds and fragmenting sea ice form open
62 coastal polynyas in the Amundsen and Ross Seas that host high phytoplankton productivity and
63 act as significant global carbon sinks (Arrigo et al., 2012). In the winter, ice cover supports the



64 turnover of deep waters that allow trace metals like Fe to be redistributed to the upper ocean
65 (Sedwick and DiTullio, 1997; Sedwick et al., 2011). Phytoplankton blooms in coastal Antarctic
66 polynyas are dominated by eukaryotes such as diatoms and the haptophyte *Phaeocystis antarctica*
67 (Arrigo et al., 1999; DiTullio et al., 2003), while cyanobacteria like *Prochlorococcus* and
68 *Synechococcus*, which are highly abundant in the adjacent South Pacific and South Atlantic gyres,
69 are near-absent from the phytoplankton community in the Southern Ocean (DiTullio et al., 2003;
70 Bertrand et al., 2011; Chandler et al., 2016).

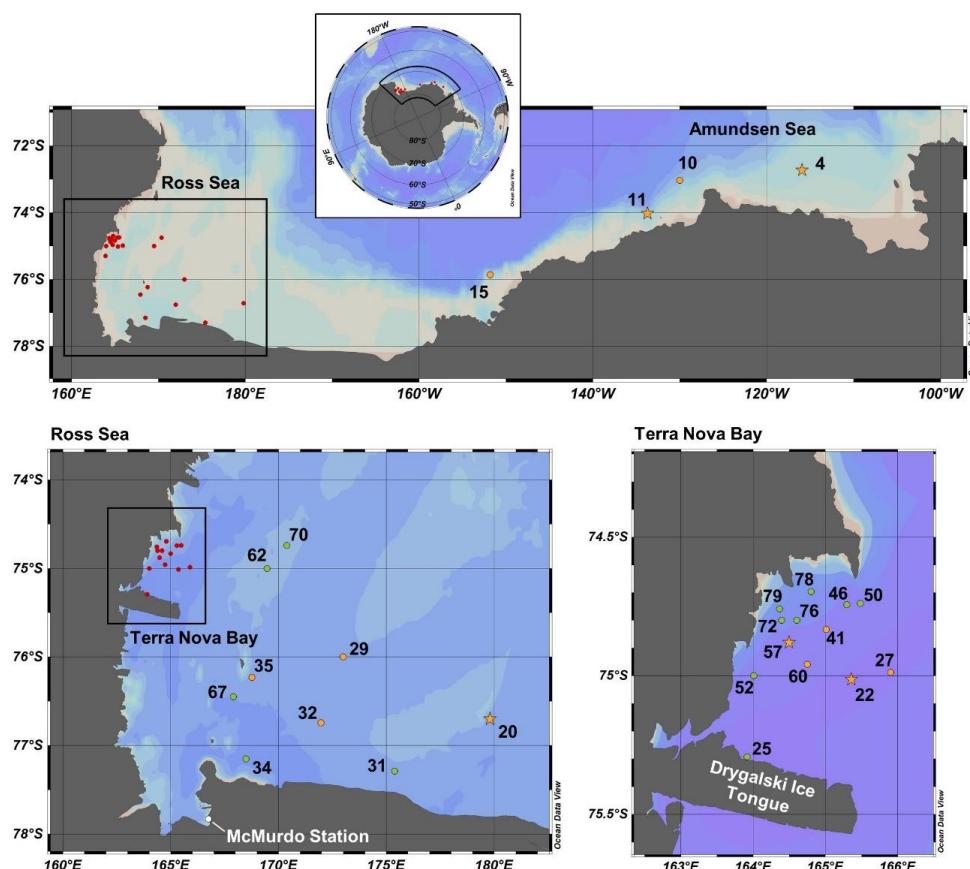
71 Cobalt (Co) is an essential trace metal nutrient for many marine plankton and is relatively
72 scarce in the marine environment, often present in the dissolved phase (dCo) in picomolar
73 concentrations (10^{-12} mol L⁻¹). Co acts as a cofactor for metalloenzymes like carbonic anhydrase,
74 a crucial enzyme in the carbon concentrating mechanism of photosynthetic phytoplankton (Sunda
75 and Huntsman, 1995; Roberts et al., 1997; Kellogg et al., 2020), and vitamin B₁₂ (cobalamin),
76 which can be used for the biosynthesis of methionine but is only produced by some bacteria and
77 archaea (Warren et al., 2002; Bertrand et al., 2013). In the Ross Sea, vitamin B₁₂ availability has
78 been observed to co-limit phytoplankton growth with iron (Fe) when bacterial abundance is low
79 (Bertrand et al., 2007). Some phytoplankton exhibit flexible vitamin B₁₂ metabolisms and can
80 express a vitamin B₁₂-independent methionine synthase pathway (*metE* gene) instead of the
81 vitamin B₁₂-dependent pathway (*metH* gene), allowing these organisms to thrive in vitamin-
82 depleted environments (Rodionov et al., 2003; Bertrand et al., 2013; Helliwell, 2017). Recently,
83 *P. antarctica* was discovered to contain both *metH* and a putative *metE* gene, displaying a
84 metabolism that is flexible to vitamin B₁₂ availability (Rao et al., [In review]). Additionally, recent
85 observations of Zn co-limitation with Fe have been documented in the Ross Sea (Kellogg et al.,
86 [Submitted]), suggesting a complex landscape of trace metal and vitamin stress interactions in the
87 otherwise macronutrient-rich waters of coastal Antarctica.

88 Dissolved Co is present as two primary species in the marine environment: a “free” labile
89 Co(II) species with weakly bound ligands and a Co(III) species that is strongly bound to organic
90 ligands ($K_s > 10^{16.8}$) (Saito et al., 2005). Labile dCo is considered to be more bioavailable to marine
91 microbes than strongly-bound dCo, although there is evidence that phytoplankton communities
92 can access Co in strongly-bound organic ligand complexes (Saito and Moffett 2001) and that
93 microbial communities may produce extracellular Co ligands that stabilize dCo and prevent its
94 loss via scavenging to manganese (Mn)-oxide particles (Saito et al., 2005; Bown et al., 2012).
95 Previous dCo sampling expeditions to the Ross Sea, including two 2005/2006 Controls of Ross
96 Sea Algal Community Structure (CORSACS) expeditions (Saito et al., 2010) and fieldwork in
97 2009 that sampled the water column below early spring sea ice in the McMurdo Sound (Noble et
98 al., 2013), reported relatively high concentrations of labile dCo in the surface Ross Sea when
99 compared to the tropical and subtropical global oceans, suggesting that labile dCo was fairly
100 replete and bioavailable to phytoplankton at the time (Saito et al., 2010).

101 This study examines the biogeochemical cycle of Co in the Amundsen and Ross Seas
102 during the 2017/2018 austral summer as part of the Cobalamin and Iron Co-Limitation of
103 Phytoplankton Species (CICLOPS) expedition. Here, we present profiles of dCo speciation that
104 revealed a lower dCo inventory during the 2017/2018 summer bloom compared to that observed
105 during the 2005/2006 CORSACS expeditions, as well as mostly undetectable concentrations of
106 labile dCo in the surface ocean. Additional datasets of dissolved zinc (dZn) and cadmium (dCd),
107 as well as profiles of Co, Zn and Cd uptake rates measured by isotope tracer incubation
108 experiments suggest that regions of vitamin B₁₂ and Zn stress within phytoplankton blooms could



109 be driving high demand for bioavailable Co in the surface ocean. The results presented by this
 110 study reveal a substantial perturbation of the Co cycle and a shift towards vitamin B₁₂ and/or Zn
 111 limitation in coastal Antarctic waters impacted by high rates of glacial ice melt and a warming
 112 climate.



113 **Figure 1.** Map of CICLOPS stations in coastal Antarctic waters, including insets of stations within
 114 the Ross Sea and Terra Nova Bay. Dissolved Co, dZn and dCd were analyzed at stations marked
 115 in yellow, and stations marked in green were analyzed for dZn and dCd, but electrochemical dCo
 116 measurements were not conducted. At stations marked with a star, Co, Zn and Cd uptake profiles
 117 are presented in this study. Stations marked in red are shown in more detail in an inset. Note that
 118 the grey coastline marks both terrestrial coastline and areas of consistent ice, including ice shelves
 119 and glaciers; this includes the Drygalski Ice Tongue, a glacier to the south of Terra Nova Bay.
 120

121 2 Methods

122 2.1 Study area and trace metal sampling

123 Samples were collected along the coastal Antarctic shelf from the Amundsen Sea, Ross
 124 Sea, and Terra Nova Bay (Fig. 1) during the CICLOPS expedition on the RVIB *Nathaniel B.*



125 *Palmer* (NBP-1801; December 16, 2017 – March 3, 2018). Dissolved seawater was collected from
126 full-depth station profiles using a trace metal clean sampling rosette deployed on a conducting
127 synthetic line supplied by the U.S. Antarctic Program (USAP) and equipped with twelve 8 L X-
128 Niskin bottles (Ocean Test Equipment) supplied by the Saito laboratory. Real-time trace metal
129 rosette operations allowed for the careful collection of seawater from 10 and 20 m above the ocean
130 floor to study sediment-water interactions within a potential nepheloid layer. After deployment,
131 the X-Niskin bottles were transported to a trace metal clean van and pressurized with high-purity
132 (99.999 %) N₂ gas. Seawater samples for nutrients, dCo and trace metal analysis were then filtered
133 through acid-washed 0.2 µM Supor polyethersulfone membrane filters (Pall Corporation, 142 mm
134 diameter) within 3 hours of rosette recovery.

135 To minimize metal contamination of samples, all sample bottles were prepared using trace
136 metal clean procedures prior to the expedition. The cleaning procedure for dCo sample bottles
137 entailed soaking sample bottles for ~1 week in Citranox, an acidic detergent, rinsing with Milli-Q
138 water (Millipore), soaking sample bottles for ~2 weeks in 10% trace metal grade HCl (Optima,
139 Fisher Scientific), and rinsing with lightly acidic Milli-Q water (< 0.1% HCl). Macronutrient
140 sample bottles were rinsed with Milli-Q water and soaked overnight in 10% HCl. The procedure
141 for total dissolved metal sample bottles (dZn and dCd) was identical to that used for dCo bottles
142 except the Citranox soak step was omitted.

143 Samples for dCo analysis were collected in 60 mL low-density polyethylene (LDPE)
144 bottles and stored at 4°C until analysis. Duplicate dCo samples were collected: one for at-sea
145 analysis of labile dCo and total dCo, and another for preservation and total dCo analysis in the
146 laboratory after the expedition. Preserved total dCo samples were stored with oxygen-absorbing
147 satchels (Mitsubishi Gas Chemical, model RP-3K), which preserve the sample for long-term
148 storage and future analysis (Noble et al., 2017; Bundy et al., 2020). Preserved dCo samples were
149 stored in groups of 6 within an open (unsealed) plastic bag, which was then placed into a gas-
150 impermeable plastic bag (Ampac) with one oxygen-absorbing satchel per 60 mL dCo sample. The
151 outer bag was then heat-sealed and stored at 4°C until analysis.

152 Samples for total dissolved metal analysis (dZn and dCd) were collected in 250 mL LDPE
153 bottles and stored double-bagged at room temperature. After ~7 months, the total dissolved metals
154 samples were acidified to a pH of 1.7 with trace metal grade HCl (Optima, Fisher Scientific), and
155 were stored acidified for more than one year before instrumental analysis.

156 2.2 Dissolved Co and labile dCo analysis

157 Total dCo – the combined fractions of labile and ligand-bound dCo, hereafter simply dCo
158 – and labile dCo concentrations were analyzed via cathodic stripping voltammetry (CSV) as
159 described by Saito and Moffett (2001) and modified by Saito et al. (2010) and Hawco et al. (2016).
160 CSV analysis was conducted using a Metrohm 663 VA and µAutolabIII systems equipped with a
161 hanging mercury drop working electrode. All reagents were prepared as described in Chmiel et al.
162 (2022). Most samples were analyzed at sea within 3 weeks of sample collection, and stations 57
163 and 60 were analyzed for labile dCo at sea and their duplicate preserved samples were analyzed
164 for total dCo in November 2019 in the laboratory.

165 To measure total dCo concentrations, filtered seawater samples were first UV-irradiated in
166 quartz tubes for one hour in a Metrohm 705 UV Digester to destroy natural ligand-bound Co
167 complexes. 11 mL of sample was then added to a 15 mL trace metal clean polypropylene vial, and



168 100 μL of 0.1 M dimethylglyoxime (DMG; Sigma Aldrich) ligand and 130 μL of 0.5 M N-(2-
169 hydroxyethyl)piperazine-N-(3-propanesulfonic acid) (EPPS, Sigma Aldrich) buffer was added to
170 each sample vial. A Metrohm 858 Sample Processor then loaded 8.5 mL of each sample into the
171 electrode's Teflon cup and added 1.5 mL of 1.5 M NaNO_2 reagent (Merck). The mercury electrode
172 performed a fast linear sweep from -1.4 V to -0.6 V at a rate of 5 V s^{-1} and produced a cobalt
173 reduction peak at -1.15 V, the voltage at which the $\text{Co}(\text{DMG})_2$ complex is reduced from Co(II) to
174 Co(0) (Saito and Moffett, 2001). The height of the Co reduction peak is linearly proportional to
175 the amount of total dCo present in the sample. Peak heights were determined by NOVA 1.10
176 software. A standard curve was created with 4 additions of 25 pM dCo to each sample, and a type-
177 I linear regression of the standard addition curve performed by the LINEST function in Microsoft
178 Excel allowed for the calculation of the initial amount of Co present in the sample.

179 When analyzing labile dCo concentrations, samples were not UV-irradiated so as to only
180 quantify the free or weakly bound dCo not bound to strong organic ligands. 11 mL of labile
181 samples were instead allowed to equilibrate with the DMG ligand and EPPS reagent overnight (~8
182 hours) before analysis to allow time for the labile dCo present in the sample to bind to the DMG
183 ligand via competitive ligand exchange ($K > 10^{16.8}$). Labile dCo samples were then loaded onto
184 the Sample Processor and analyzed electrochemically using identical methods as described above
185 for total dCo samples.

186 2.3 Dissolved Co standards and blanks

187 During the CICLOPS expedition, an internal standard consisting of filtered, UV-irradiated
188 seawater was analyzed for dCo every few days while samples were being analyzed ($39 \pm 4 \text{ pM}$, n
189 $= 9$). While additional preserved dCo samples were analyzed in the laboratory in November 2019,
190 triplicate GSC2 GEOTRACES community intercalibration standards were carefully neutralized to
191 a pH of ~8 using negligible volumes of ammonium hydroxide (NH_4OH) and analyzed for dCo.
192 This is the same intercalibration batch originally reported in Table 1 of Chmiel et al. (2022), as
193 analysis for both expeditions overlapped temporally. The GSC2 standard was determined to have
194 a dCo concentration of 80.2 ± 6.2 ($n = 3$), a value that is very similar to the one reported by Hawco
195 et al., (2016) (77.7 ± 2.4). Currently, no official community consensus for dCo in the GSC2
196 intercalibration standard exists.

197 Analytical blank measurements for each reagent batch (a unique combination of DMG,
198 EPPS, and NaNO_2 reagent batches) were measured to determine any Co contamination due to
199 reagent impurities. Blanks were prepared in triplicate with UV-irradiated surface seawater passed
200 through a column with Chelex 100 resin beads (Bio-Rad) to remove metal contaminants, then UV-
201 irradiated again. Chelex beads were prepared as described in Price et al. (2013) to remove organic
202 impurities from leaching into the eluent. For the 5 batches of reagents used on this expedition, the
203 analytical blanks were found to be 2.3 pM, 4.0 pM, 10.1 pM, 15.6 pM, and 8.6 pM dCo, with an
204 average of 8.1 pM Co. The analytical blank detected for the laboratory-run total dCo samples was
205 1.0 pM. It should be noted that blank values above 10 pM are considered high for this method.
206 Analytical blank values were subtracted from the measured Co values determined with the
207 respective reagent batch. The average standard deviation within each triplicate batch of blanks (1.3
208 pM) was used to estimate the analytical limit of detection ($3 \times$ blank standard deviation) of 4 pM.
209 When detectable dCo concentrations were found below the 4 pM detection limit, their values were
210 preserved in the dataset and flagged as below the detection limit (<DL). In cases where no dCo or
211 labile dCo were detected (i.e., when no peak was measurable and/or the dCo value predicted was



212 < 0 pM), values of 0 pM were assigned for the purposes of plotting and selecting statistical analysis
 213 and were flagged as not detected (n.d.) as well as <DL in the dataset; although these concentrations
 214 were not detectable with our methodology, we believe the incredibly low concentrations of dCo
 215 and labile dCo observed on this expedition were meaningful, and that removing these values from
 216 our analysis misrepresents the data and would skew the results to appear higher than was observed.

217 **Table 1.** Mean dCo and labile dCo values measured in the surface ocean (10 m) and the deep
 218 ocean (> 100 m) in the three regions sampled. One dCo sample and numerous labile dCo samples
 219 were determined to be below the analytical detection limit (<DL) of 4 pM. Only using the values
 220 measured above the detection limit would artificially inflate the calculation of the mean value;
 221 instead, samples measured between 0 and the DL were left unaltered as their originally measured
 222 value and samples with no detected concentrations of dCo or labile dCo (n.d.) were adjusted to 0
 223 pM. The number of samples included in the mean calculation that are <DL is indicated by n_{<DL}.
 224

Surface (10 m)					
Region	n	dCo _{mean} [pM]	n _{<DL} for dCo	Labile dCo _{mean} [pM]	n _{<DL} for labile dCo
Amundsen Sea	4	28 ± 7	0	5 ± 6	2
Ross Sea	4	28 ± 12	0	1 ± 2 ^a	4
Terra Nova Bay	5	11 ± 7	1	n.d. ^b	5
Deep (> 100 m)					
Region	n	dCo _{mean} [pM]	n _{<DL}	Labile dCo _{mean} [pM]	Labile dCo n _{<DL}
Amundsen Sea	30	41 ± 5	0	4 ± 4	14
Ross Sea	32	46 ± 8	0	9 ± 7	9
Terra Nova Bay	34	39 ± 18	0	6 ± 8	18

225
 226 ^a Of the 4 surface samples analyzed for labile dCo in the Ross Sea, 3 were n.d. and the fourth
 227 contained 3.5 pM labile dCo.

228 ^b All surface samples in Terra Nova Bay were n.d. for labile dCo.

229 2.4 Dissolved Zn and Cd analyzed by ICP-MS

230 Total dissolved trace metal samples were analyzed for dZn and dCd using isotope dilution
 231 and inductively coupled plasma mass spectrometry (ICP-MS) as described in Kellogg et al.
 232 (Submitted) based on methodology described in Cohen et al. (2021). Briefly, 15 mL of acidified
 233 filtered seawater samples were spiked with an acidified mixture of stable isotopes including ⁶⁷Zn,
 234 and ¹¹⁰Cd, among other metal stable isotopes, and pre-concentrated via a solid phase extraction
 235 system seaFAST-pico (Elemental Scientific) to an elution volume of 500 µL. The samples were
 236 then analyzed using an iCAP-Q ICP-MS (Thermo Scientific) and concentrations were determined
 237 using a multi-elemental standard curve (SPEX CertiPrep).

238 2.5 Co, Zn and Cd uptake rates via isotope incubations

239 Co, Zn and Cd uptake rates were quantified using incubations of collected marine microbial
 240 communities spiked with stable or radioisotopes to trace the conversion of dissolved trace metal
 241 into the particulate phase. Briefly, unfiltered seawater used for the incubation uptake experiments
 242 was collected from the trace metal rosette, and the Co, Zn and Cd uptake incubations were spiked



243 with 0.1 pM $^{57}\text{CoCl}_2$, 2 nM ^{67}ZnO and 300 pM ^{110}CdO , respectively. All incubation bottles were
244 then sealed and placed in a flow-through shipboard incubator for 24 hours. The incubator was
245 shielded by black mesh screening to allow 20% ambient light penetration. Incubation biomass was
246 collected by vacuum filtration onto acid-rinsed 3 μm Versapor filters (Pall). The ^{57}Co incubation
247 filters were stored at room temperature in Petri dishes prior to radiochemical gamma-ray counting
248 both at sea and in the laboratory, and the ^{67}Zn and ^{110}Cd incubation filters were stored at $-80\text{ }^\circ\text{C}$ in
249 acid-rinsed cryovials until ICP-MS analysis in the laboratory. See Kellogg et al. (Submitted), Rao
250 2020 and Kellogg (2022) for full methodology and instrumental analysis.

251 2.6 Pigment and phosphate analysis

252 Phytoplankton pigment samples were collected via filtration and analyzed for select
253 pigments by high-performance liquid chromatography (HPLC) as described in DiTullio and
254 Geesey (2003). Macronutrient samples were collected from the trace metal rosette alongside dCo
255 samples and were filtered using the same methodology as dCo and total metal samples (see above).
256 Samples were collected in 60 mL high-density polyethylene (HDPE) bottles and were stored
257 frozen until analysis. Dissolved PO_4 concentrations were determined by Joe Jennings at Oregon
258 State University via the molybdenum blue method (Bernhardt and Wilhelms, 1967) using a
259 Technicon AutoAnalyzer II attached to an Alpkem autosampler.

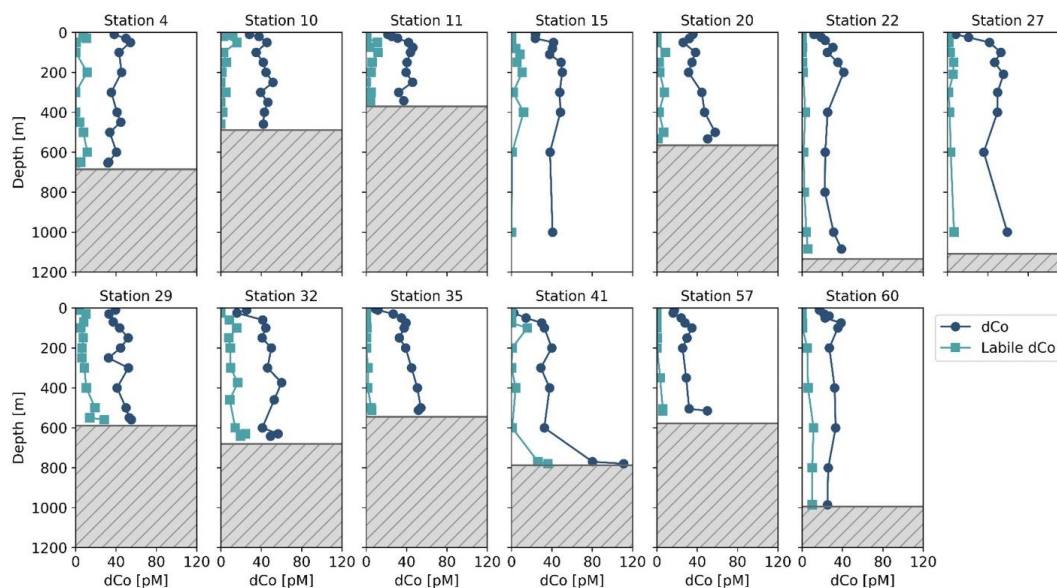
260 2.7 Historical dCo and pigment data

261 In this study, dCo profiles from the CICLOPS expedition are compared to those from
262 previous fieldwork in the Ross Sea, including the Controls of Ross Sea Algal Community Structure
263 (CORSACS) expeditions: CORSACS-1 (NBP-0601; December 27, 2005 – January 23, 2006) and
264 CORSACS-2 (NBP-0608; November 8, 2006 – December 3, 2006), reported in Saito et al. (2010),
265 and fieldwork sampling the water column under the sea ice of the McMurdo Sound (November 9
266 – 23, 2009), reported in Noble et al. (2013). Dissolved cobalt and pigment data from these three
267 fieldwork expeditions were sampled and analyzed with comparable methodologies as those used
268 on the CICLOPS expedition, and the CORSACS data are accessible online at [https://www.bco-](https://www.bco-dmo.org/dataset/3367)
269 [dmo.org/dataset/3367](https://www.bco-dmo.org/dataset/3367).

270 2.8 Statistical Analysis

271 The linear regressions presented in this study are two-way (type-II) linear regressions, with
272 the exception of the standard addition curves used to calculate dCo concentrations (Sect. 2.2).
273 Two-way regressions are ideal for stoichiometric ratios because they allow for error in both the x
274 and y parameters and do not assume dependence between the x and y axes. The two-way regression
275 function used in this study was rewritten to Python from a MATLAB file (lsqfitma.m) originally
276 written by Ed Pelzer circa 1995 (Chmiel et al., 2022) and is available at [https://github.com/rebecca-](https://github.com/rebecca-chmiel/GP15)
277 [chmiel/GP15](https://github.com/rebecca-chmiel/GP15).

278 Independent t-tests were performed using the stats.ttest_ind function within statistical
279 function module of the SciPy Python library.



280

281

282

283

Figure 2. Dissolved Co and labile dCo full-depth profiles from the CICLOPS expedition to the Amundsen Sea (Stations 4, 10, 11, 15), Ross Sea (Stations 20, 29, 32, 35) and Terra Nova Bay (Stations 22, 27, 41, 57, 60). The top of the grey box marks the location of the seafloor.

284

3 Results

285

3.1 Dissolved Co distribution and speciation

286

287

288

289

290

291

292

293

294

295

296

During the CICLOPS expedition, full-depth profiles of dCo and labile dCo samples were analyzed from 13 stations in the Amundsen Sea (Stations 4, 10, 11, 15), the Ross Sea (Stations 20, 29, 32, 35) and Terra Nova Bay (Stations 22, 27, 41, 57, 60; Fig. 1). The resulting dCo profiles (Fig. 2) show depletion in the surface ocean consistent with a nutrient-type profile; at 10 m depth, dCo concentrations were found to be 28 ± 7 pM in the Amundsen Sea ($n = 4$), 28 ± 12 pM in the Ross Sea ($n = 4$), and only 11 ± 7 pM in Terra Nova Bay ($n = 5$; Table 1). Labile dCo distributions generally followed those of dCo, and also showed strong depletion in the surface ocean. In the Amundsen and Ross Seas, surface (~ 10 m) labile dCo concentrations ranged between 12 pM at station 10 and undetected (n.d.) concentrations at stations 15, 20, 32 and 35. In Terra Nova Bay, no surface labile dCo concentrations were detected at any of the 5 stations sampled, indicating that the dCo inventory was dominated by the strongly ligand-bound dCo fraction.

297

298

299

300

301

302

303

304

305

In the deep ocean (≥ 100 m depth), dCo distributions were relatively consistent throughout the water column, with the exception of elevated concentrations of dCo at near-bottom depths. The Amundsen Sea, Ross Sea, and Terra Nova Bay all displayed similar deep (≥ 100 m depth) dCo concentrations of 41 ± 5 pM ($n = 30$), 46 ± 8 pM ($n = 32$), and 39 ± 18 pM ($n = 34$), respectively (Table 1). The high standard deviation of deep dCo in Terra Nova Bay is partially driven by the elevated near-seafloor signal at Station 41; when the two deepest points at Station 41 are omitted (770 m and 780 m), the average deep dCo in Terra Nova Bay was 36 ± 10 pM. The CICLOPS expedition included regular near-bottom sampling as allowed by the altimeter aboard the trace metal rosette. As a result, many of the deepest profile samples contained elevated concentrations



306 of dCo and labile dCo along the seafloor, including stations 20, 22, 27, 29, 32, 41 and 57. This
307 deep dCo signal was particularly observable in stations where two near-seafloor samples were
308 taken: one ~10 m above the seafloor and a second ~20 m above the seafloor. At stations 41 and
309 57, the elevated near-seafloor dCo signal was pronounced (Fig. 2); the samples ~10 m above the
310 seafloor contained 111 pM and 50 pM dCo, respectively, which represents a 31 pM and 18 pM
311 increase, respectively, from the samples collected ~20 m above the seafloor. This finding indicates
312 that dCo was elevated in a narrow band close to the seafloor, and it is likely that dCo concentrations
313 continued to increase in the 10 m between the deepest samples and the seafloor.

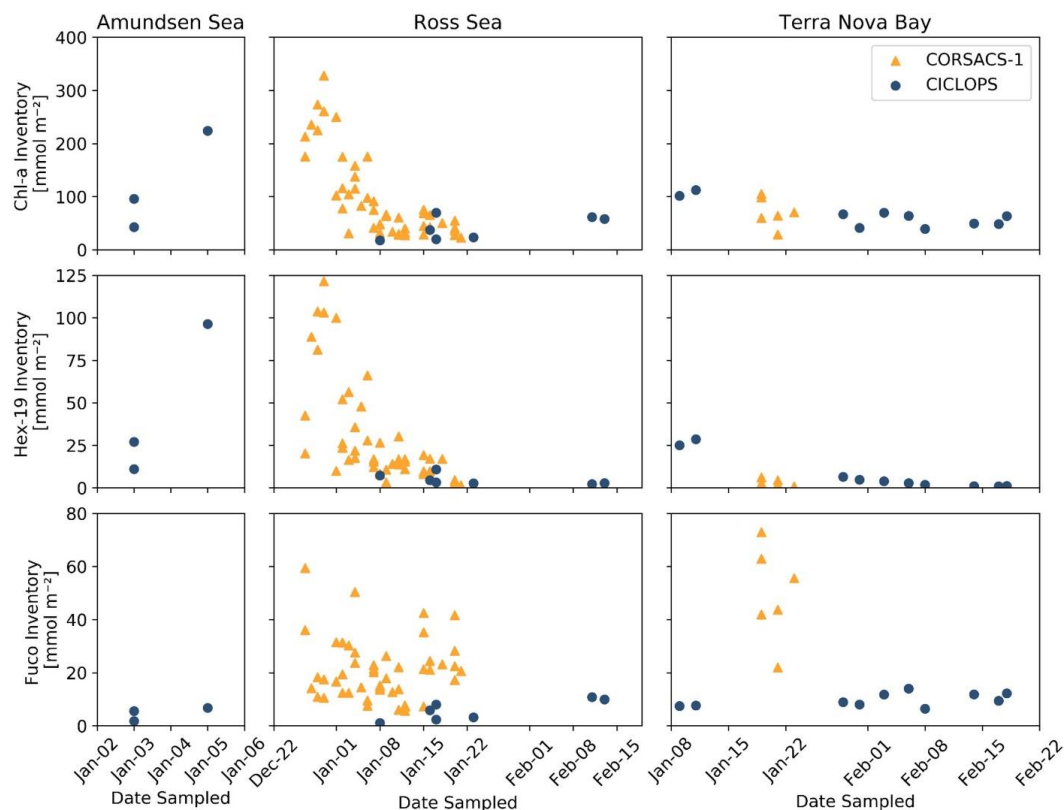
314 3.2 Phytoplankton communities in the Amundsen Sea, Ross Sea and Terra Nova Bay

315 Stations 11, 15, 22 and 27 exhibited high surface chlorophyll-a (Chl-a) fluorescence (17–
316 42 mg m⁻³ at 10 m), characteristic of phytoplankton blooms. The Amundsen Sea stations displayed
317 high concentrations of 19'-hexanolyoxyfucoxanthin (19'-Hex), a pigment commonly used as a
318 proxy for haptophyte biomass. In the coastal Southern Ocean, 19'-Hex is often correlated with
319 *Phaeocystis antarctica* (DiTullio and Smith, 1996; DiTullio et al., 2003), and it is typical to find
320 concentrated blooms of *P. antarctica* in these regions, particularly during the highly productive
321 spring blooms of the Antarctic polynyas (Arrigo et al., 1999; DiTullio et al., 2000). The pigment
322 fucoxanthin (Fuco) is commonly used as a proxy for diatom biomass, although it can also be
323 produced by haptophytes like *P. antarctica* growing under Fe-replete conditions (DiTullio et al.,
324 2003; DiTullio et al., 2007); Fuco was observed at stations throughout the expedition and tended
325 to be relatively consistent throughout the CICLOPS stations, particularly in comparison to 19'-
326 Hex, which displayed very high concentrations at some stations and much lower concentrations at
327 others. In general, higher concentrations of Fuco were observed within Terra Nova Bay as well as
328 at stations sampled later in the summer season. This is consistent with past observations of summer
329 diatom blooms, which tend to occur after the annual spring bloom where and when dFe is available
330 (Sedwick et al., 2000; Peloquin and Smith, 2007; Saito et al., 2010).

331 The upper ocean inventories of three pigments, 19'-Hex, Fuco and Chl-a, a proxy for
332 general phytoplankton biomass in the Southern Ocean, were estimated via trapezoidal integration
333 of their profiles between 5 and 50 m depth and compared to the 2005/2006 summer bloom
334 observed on the CORSACS-1 expedition (Fig. 3). In the Ross Sea and Terra Nova Bay, CICLOPS
335 stations contained smaller inventories of Chl-a and 19'-Hex compared to the Amundsen Sea, likely
336 reflecting the end of the spring bloom and transition to a summer phytoplankton assemblage in
337 these regions. One noticeable difference between the overlapping 2006 and 2018 January seasons
338 is the larger Fuco inventory in 2006 in both the Ross Sea and Terra Nova Bay compared to the
339 2018 season, indicating a larger presence of diatom biomass during the CORSACS-1 expedition
340 compared to the CICLOPS expedition despite relatively similar Chl-a inventories.

341 3.3 dZn, dCd and trace metal uptake rates

342 Dissolved Cd and Zn profiles, as well as trace metal uptake rate (ρ M) profiles for Co, Zn
343 and Cd from the CICLOPS expedition were originally presented in Rao (2020) and Kellogg
344 (2022). This study presents a comparison between dCo distribution and the distribution and uptake
345 of dZn and dCd, two trace metals linked with Co biogeochemical cycling since all three metals are
346 known to share similar uptake transporter pathways and can be interchangeably utilized as
347 cofactors within specific classes of the enzyme carbonic anhydrase (Sunda and Huntsman, 1995,
348 2000; Saito and Goepfert, 2008; Kellogg et al., 2020, 2022).



349
 350 **Figure 3.** Upper ocean inventories of Chlorophyll-a (Chl-a), 19'-
 351 Hex) and fucoxanthin (Fuco) plotted over the austral summer season for both the 2005/2006
 352 CORSACS-1 and 2017/2018 CICLOPS expeditions. Inventories were estimated via trapezoidal
 353 integration of the pigment depth profiles between 5 and 50 m depth. Note that the dates along the
 354 x-axis are not continuous between plots of each region, and the y-axis scales differ among the 3
 355 pigments.

356 The dZn and dCd profiles observed on the CICLOPS expedition displayed nutrient-like
 357 structure, with depleted concentrations near the surface (Fig. 4). In the deep ocean (≥ 100 m), dZn
 358 and dCd concentrations were relatively uniform, displaying average deep concentrations of $4.6 \pm$
 359 1.1 pM ($n = 182$) and 700 ± 90 pM, respectively (Table 2). Average dissolved metal concentrations
 360 in the surface ocean (10 m depth) were higher in the Amundsen Sea (2.5 ± 1.2 nM dZn; 450 ± 170
 361 pM Cd) compared to the Ross Sea (1.1 ± 1.2 nM dZn; 250 ± 170 pM dCd) and Terra Nova Bay
 362 (0.87 ± 0.42 nM dZn; 130 ± 170 pM dCd). This trend of decreasing surface dissolved metals from
 363 the Amundsen to Terra Nova Bay was mirrored in the dCo distributions, and could be explained
 364 by the seasonal drawdown of metal nutrients in the mixed layer over time, differences in the metal
 365 uptake of phytoplankton in the different regions, or both phenomenon occurring simultaneously.

366 At Stations 4, 11, 20, 22 and 57, uptake rates of Co, Zn and Cd within surface seawater
 367 collected from 0–200 m were determined via spiked-isotope incubations (Rao, 2020; Kellogg,
 368 2022). The relative ratios of the resulting uptake profiles from biomass collected onto 3 μ m filters



369 provide insight into the demand for Co, Zn and Cd of eukaryotic phytoplankton in coastal
 370 Antarctica (Fig. 5). Note that Co uptake within the bacterial size fraction (0.2–3 μm) was also
 371 analyzed and the results are presented in Rao (2020), but here we present the results of the
 372 eukaryotic size fraction ($> 3 \mu\text{m}$) to best represent the eukaryotic phytoplankton community
 373 present and compare to the Zn and Cd uptake experiments. It should be noted that uptake rates
 374 measured via tracer addition and shipboard incubations represent potential uptake and may be
 375 overestimations of the environmental nutrient uptake rates because the isotope tracer addition was
 376 labile – not at equilibrium with the natural seawater ligands – and could have perturbed the
 377 natural micronutrient inventories. The $^{57}\text{CoCl}_2$ addition (0.1 μM) was likely a small enough
 378 addition that the inventory was not significantly disturbed, but added concentrations of ^{67}ZnO (2
 379 nM) and ^{110}CdO (300 μM) spikes were not tracer-level additions and necessarily increased the
 380 existing trace metal inventories, possibly leading to the overestimation of total metal uptake rates
 381 (Rao, 2020; Kellogg, 2022).

382 **Table 2.** Mean dZn and dCd values from the surface ocean (10 m) and the deep ocean ($> 100 \text{ m}$)
 383 in the three regions sampled.

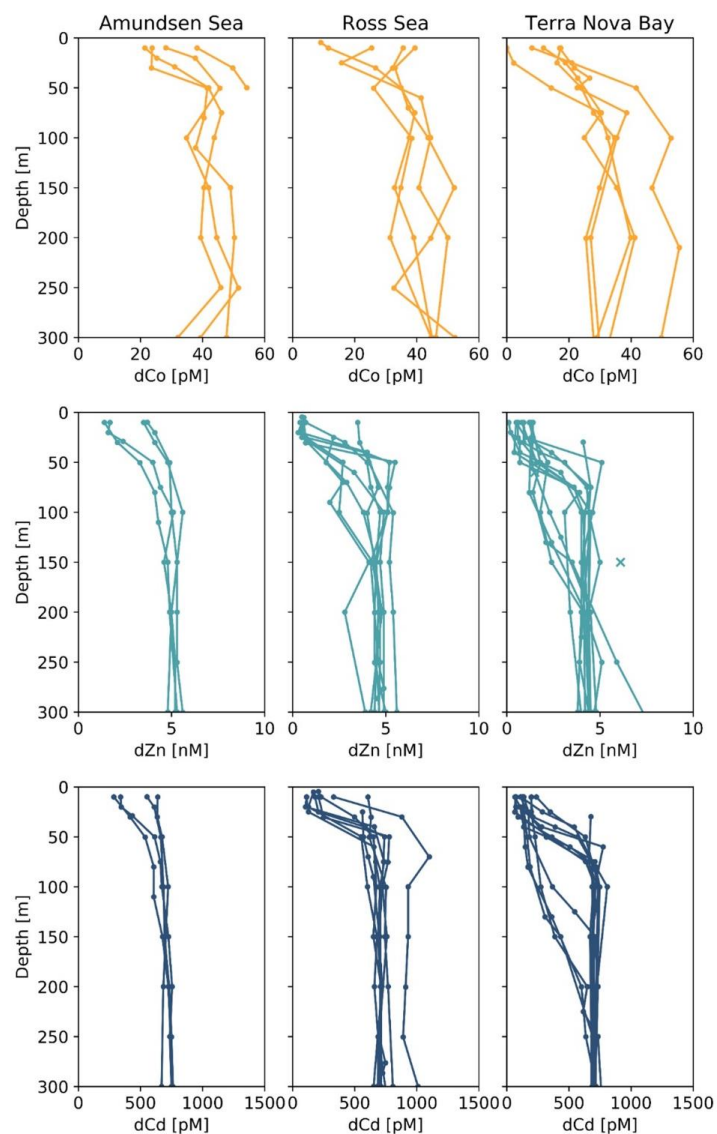
Surface (10 m)				
Region	dZn _{mean} [nM]	n _{dZn}	dCd _{mean} [pM]	n _{dCd}
Amundsen Sea	2.6 ± 1.2	4	450 ± 170	4
Ross Sea	1.1 ± 1.2	6	250 ± 170	7
Terra Nova Bay	0.87 ± 0.42	11	130 ± 60	11
All	1.3 ± 1.0	21	230 ± 170	22
Deep (> 100 m)				
Region	dZn _{mean} [nM]	n _{dZn}	dCd _{mean} [pM]	n _{dCd}
Amundsen Sea	5.4 ± 0.6	30	730 ± 40	30
Ross Sea	4.7 ± 0.6	65	740 ± 80	65
Terra Nova Bay	4.3 ± 1.4	87	670 ± 100	90
All	4.6 ± 1.1	182	700 ± 90	185

384

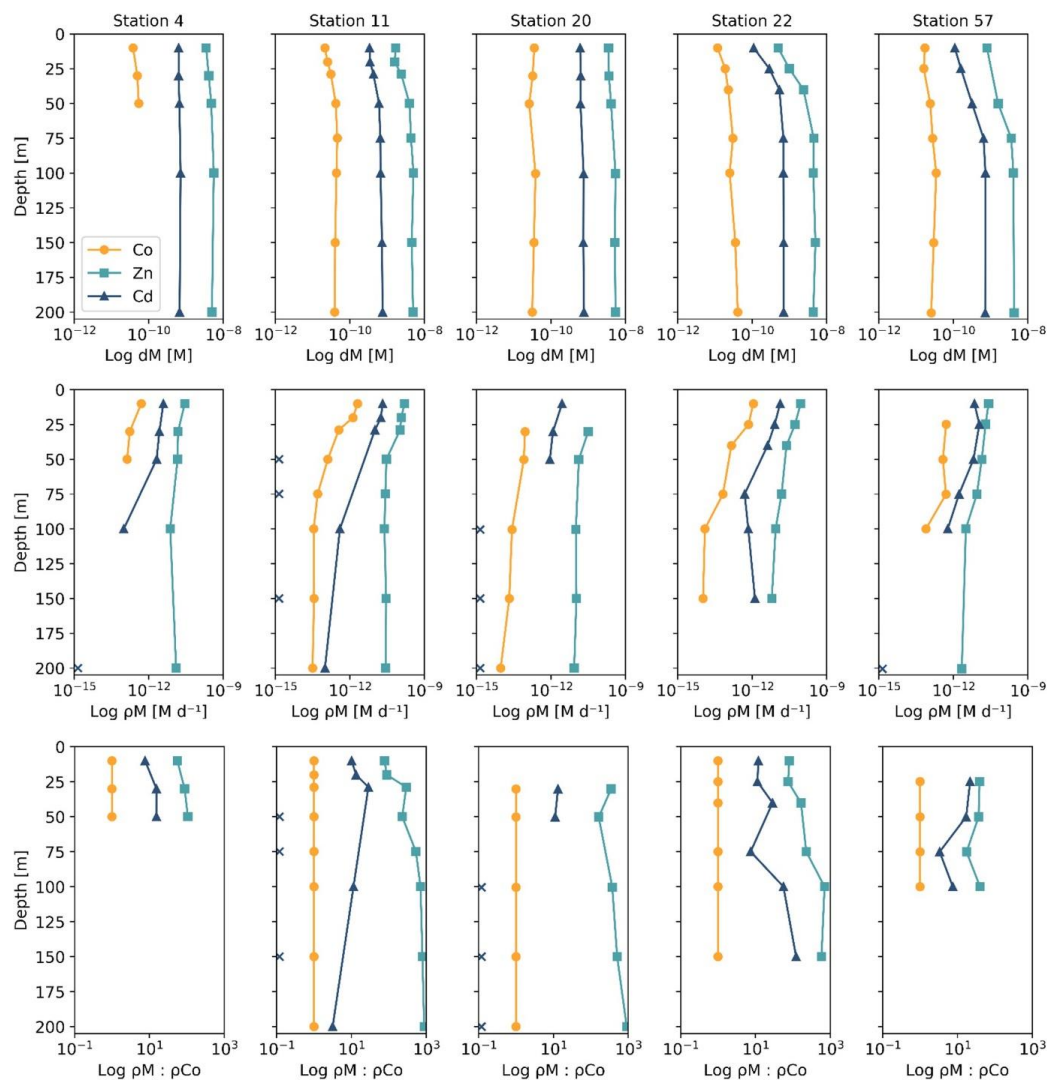
385 Of the five stations with uptake rate data from all three trace metals of interest, four
 386 (Stations 4, 11, 20 and 22) were from a transect conducted from the Amundsen Sea to Terra Nova
 387 Bay, and were sampled within a span of 10 days from December 31, 2017 to January 9, 2018,
 388 while the last station (Station 57) was sampled later in the summer on February 6, 2018; this range
 389 of stations allows us to assess the uptake stoichiometry along both spatial (location) and time
 390 (bloom progression) dimensions. The ρM profiles displayed an increase in metal uptake of Co, Zn
 391 and Cd towards the surface, a shape which was mirrored in the lower dissolved trace metal
 392 concentrations of the surface ocean, suggesting the influence of phytoplankton uptake on the
 393 drawdown of micronutrients in the photic zone. The stoichiometry of ρM among Co, Zn and Cd
 394 tended to directly follow the metals' availability as dissolved species: Co, which is present at
 395 the lowest concentrations of $\sim 10^{-11} \text{ M}$, was taken up at rates ranging between 10^{-13} and $10^{-12} \text{ M d}^{-1}$;
 396 Cd, at concentrations of $\sim 10^{-10} \text{ M}$, was taken up at rates of 10^{-12} to $10^{-11} \text{ M d}^{-1}$; and Zn, present in
 397 the highest concentration of $\sim 10^{-9} \text{ M}$, was taken up at rates of 10^{-12} to $10^{-10} \text{ M d}^{-1}$. This observation



398 reveals order-of-magnitude differences in biological uptake between the three metals, matching
399 patterns of metal availability in the water column.



400 **Figure 4.** Upper ocean trace metal depth profiles of dCo, dZn and dCd, by region (left panels,
401 Amundsen Sea; middle panels, Ross Sea; right panels, Terra Nova Bay). Outliers are marked with
402 an 'x'. Dissolved Zn and Cd profile data are further described in Kellogg (2022).
403



404

405

406

407

408

409

410

Figure 5. Depth profiles of dissolved metals (dM; top), trace metal uptake rates (ρM ; middle), and trace metal uptake rates normalized to the uptake rate of dCo ($\rho M : \rho Co$), plotted along a log scale. Stations 4 and 11 are from the Amundsen Sea, Station 20 is from the Ross Sea, and Stations 22 and 57 are from Terra Nova Bay. Depths at which an uptake rate below detection (specifically for ρCd) are marked with an 'x' along the y-axis. Co trace metal uptake data are further described in Rao (2020) and Zn and Cd uptake data are further described in Kellogg (2022).

411

4 Discussion

412

4.1 Biogeochemical Co cycle processes observed via dCo profiles and dCo : dPO₄³⁻ stoichiometry

413

Low surface ocean dCo and labile dCo concentrations are attributable to uptake by phytoplankton and bacteria in the Southern Ocean, giving the dCo and labile dCo profiles a distinct

414



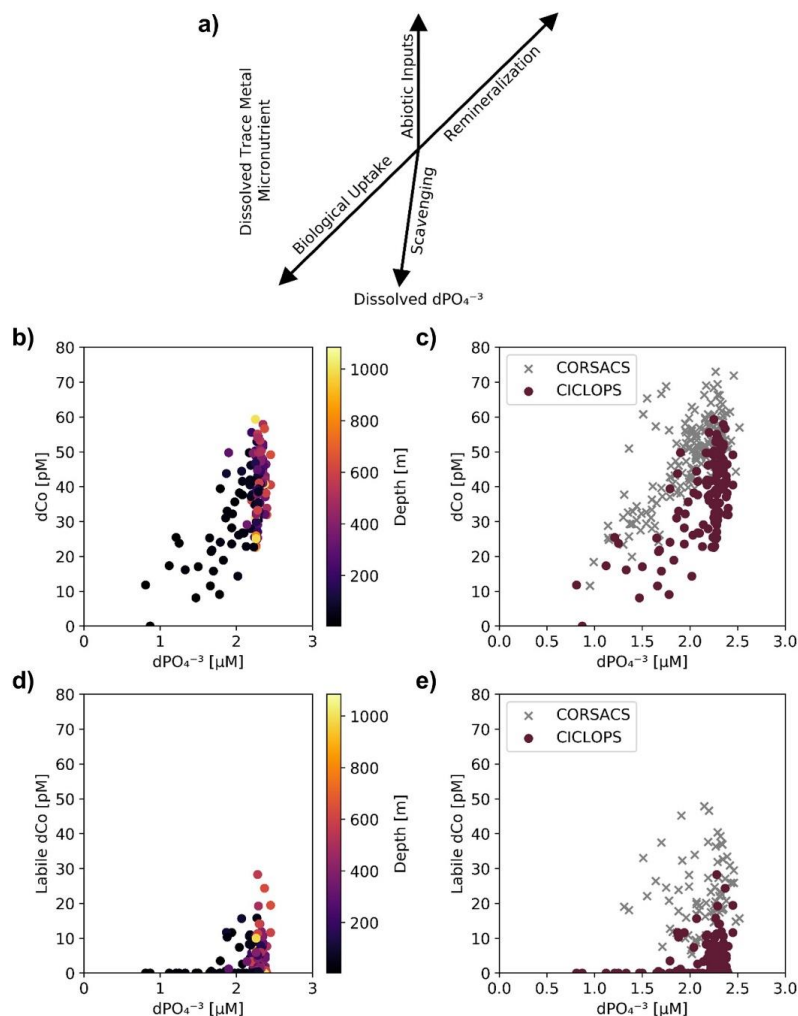
415 nutrient-like shape (Fig. 2). The labile dCo fraction was extremely low or below the limit of
416 detection in surface waters, particularly within Terra Nova Bay, indicating strong drawdown of
417 the labile fraction and near 100% complexation of dCo in the water column. Labile dCo is
418 considered to be more bioavailable than strongly-bound dCo and thus is likely preferentially taken
419 up by microbes when available. This labile dCo may then be rapidly cycled by phytoplankton in
420 the mixed layer and any labile dCo released via remineralization, cell lysis, or grazing would be
421 promptly taken up by other algae and microbes. A rapid turnover of labile dCo suggests a high
422 demand for bioavailable Co from the surface phytoplankton community.

423 Dissolved Co and PO₄ displayed a generally positive relationship in the upper ocean, which
424 is indicative of the co-cycling of both nutrients via phytoplankton uptake and remineralization
425 (Fig. 6a). The processes of biological uptake and remineralization, when observed along dCo vs.
426 dPO₄³⁻ axes, can be represented by vectors with positive slopes and opposite directionality. Abiotic
427 dCo inputs and Co scavenging processes can be represented by vertical or near-vertical vectors
428 because they decouple the cycling of dCo and dPO₄³⁻. The positive dCo vs. dPO₄³⁻ linear
429 relationship that is often observed within the ocean's mixed layer can exhibit a variety of slopes
430 that are dictated by the nutrient uptake and remineralization stoichiometry of the microbial
431 community (Saito et al., 2017). On CICLOPS, the dCo vs. dPO₄³⁻ relationship displayed a
432 drawdown of both dCo and dPO₄³⁻ in the upper ocean, and the labile dCo vs. dPO₄³⁻ relationship
433 revealed the stark lack of labile dCo throughout the upper ocean (Fig. 6b,d). The dCo vs. dPO₄³⁻
434 slope in the upper ocean (0–100 m depth) was found to be distinct for each of the three regions
435 sampled on the expedition; the Ross Sea displayed the highest slope ($74 \pm 18 \mu\text{mol} : \text{mol}$), followed
436 by the Amundsen Sea ($47 \pm 9 \mu\text{mol} : \text{mol}$) and Terra Nova Bay, which displayed the lowest dCo
437 vs. dPO₄³⁻ slope ($26 \pm 4 \mu\text{mol} : \text{mol}$; Fig. 7; Table 3). These slopes reflect a relatively wide range
438 of dCo stoichiometries that vary by a factor of 2.8 between the lowest and highest slopes observed.
439 For comparison, the 2005/2006 CORSACS-1 and CORSACS-2 Ross Sea data points were pooled
440 and the dCo vs. dPO₄ slope was recalculated (originally reported as $37.6 \mu\text{mol} : \text{mol}$ between 5–
441 500 m depth; Saito et al., 2010) to fall within the same depth window (0–100 m). The resulting
442 slope fell within the range of slopes observed on CICLOPS ($49 \pm 4 \mu\text{mol} : \text{mol}$; $R^2 = 0.57$; $n =$
443 106).

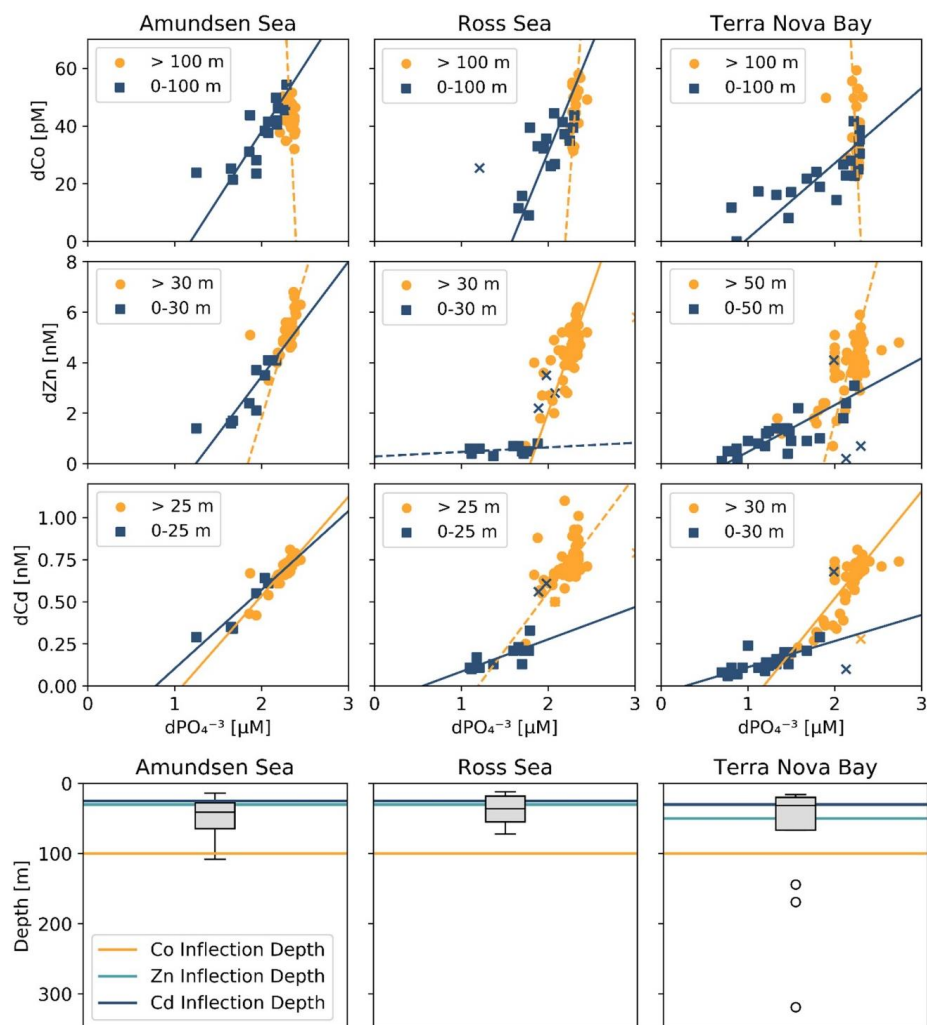
444 The range of dCo vs. dPO₄³⁻ slopes reflects the elasticity of cobalt uptake stoichiometry in
445 the upper ocean, which varies by microbial community and the availability of dCo and other
446 nutrients. Due to the number of factors that can affect the environmental stoichiometry of trace
447 metal nutrients, the dCo vs. dPO₄³⁻ slope must be interpreted alongside other information about
448 the marine environment, such as the available dCo inventory and the local nutrient limitation
449 regime, making global comparisons of dCo : dPO₄³⁻ stoichiometry complex. The lower
450 stoichiometric slope observed in Terra Nova Bay compared to the Ross and Amundsen Seas likely
451 indicates not a lack of demand for Co by phytoplankton, but the low availability of Co in the
452 surface ocean despite high demand for the metal. Terra Nova Bay was found to have the lowest
453 average surface dCo, dZn and dCd concentrations of the three regions studied, and both Terra
454 Nova Bay stations where ρCo was measured (Stations 22 and 57) displayed higher surface Co
455 uptake rates (0.71 and 0.51 pM d^{-1} , respectively, at 25 m depth) than Station 20 in the Ross Sea
456 (0.09 pM d^{-1} at 30 m depth). It is likely that the lower dCo stoichiometry in Terra Nova Bay was
457 driven by nutrient draw-down and low availability of labile dCo in the region resulting from
458 productive phytoplankton blooms. Remineralization would also have played a role in setting the
459 dCo vs. dPO₄ slope below the photic zone; a remineralization vector with a relatively low slope
460 indicates that there was a lower dCo source from particulate Co biomass and a rapid turnover of



461 recycled dCo back into biomass, suggesting a tight coupling of the dissolved and particulate
 462 phases.



463 **Figure 6. (a)** A vector schematic of the relationship between dPO₄³⁻ and dissolved trace metals
 464 like dCo, and how the various marine processes can affect their distribution and environmental
 465 stoichiometry. Adapted from Noble et al. (2008). The CICLOPS (b) dCo vs. dPO₄³⁻ relationship
 466 and (d) labile dCo vs. dPO₄³⁻ relationship, plotted by depth. Also shown are the CICLOPS (red)
 467 (c) dCo vs. dPO₄³⁻ and (e) labile dCo vs. dPO₄³⁻ samples overlaid with CORSACS (gray) samples.
 468



469
 470 **Figure 7.** (Top 3 rows) Trace metal : dPO_4^{3-} relationships from the three CICLOPS regions
 471 sampled, divided into upper ocean (blue square) and deep ocean (orange circle) bins with a manual
 472 depth threshold (or inflection point depth) selected to optimize the linear fit of the upper and deep
 473 ocean trends. Regressions with an $R^2 \geq 0.50$ are shown as a solid line, and those with an $R^2 < 0.50$
 474 are shown as a dotted line. The results of the linear regressions are given in Table 3. Regression
 475 outliers are marked with an 'x'. (Bottom row) The inflection point depths assigned to dCo, dZn
 476 and dCd relationships are shown compared to a box and whiskers plot of the mixed layer depths,
 477 with mixed layer depth outliers marked with an 'o'.

478

479

480



481 **Table 3.** Trace metal : dPO_4^{3-} stoichiometric regressions for dCo, dZn and dCd in both the surface
 482 and deep ocean of the Amundsen Sea, Ross Sea and Terra Nova Bay, as shown in Fig. 7. Linear
 483 regression slopes with $R^2 < 0.50$ are not shown as the slope values should not be considered
 484 meaningful stoichiometric values.
 485

Region	$dCo:dPO_4^{3-}$ [$\mu mol: mol$]				$dZn:dPO_4^{3-}$ [$mmol: mol$]				$dCd:dPO_4^{3-}$ [$mmol: mol$]			
	Depths [m]	n	Slope	R^2	Depths [m]	n	Slope	R^2	Depths [m]	n	Slope	R^2
Amundsen Sea												
Surface	0-100	16	47 ± 9	0.64	0-30	9	4.6 ± 0.9	0.72	0-25	6	0.47 ± 0.08	0.86
Deep	>100	20	--	0.02	>30	35	--	0.37	>25	38	0.59 ± 0.06	0.72
Ross Sea												
Surface	0-100	15	74 ± 18	0.53	0-30	11	--	0.07	0-25	11	0.19 ± 0.05	0.56
Deep	>100	24	--	0.21	>30	77	9.8 ± 1.0	0.54	>25	79	--	0.26
Terra Nova Bay												
Surf	0-100	20	26 ± 4	0.65	0-50	24	1.9 ± 0.3	0.65	0-30	21	0.15 ± 0.03	0.59
Deep	>100	26	--	0.05	>50	95	--	0.30	>30	104	0.64 ± 0.03	0.80

487 Deviations from the linear uptake-remineralization line in the dCo vs. dPO_4^{3-} relationship
 488 occur when dCo distributions become decoupled from dPO_4^{3-} or vice versa, as with Co scavenging
 489 onto particles and lithogenic dCo sources. In other ocean regions, the dCo vs. dPO_4^{3-} relationship
 490 displays a characteristic “curl” towards the high- dPO_4^{3-} , low-dCo in deeper waters, resulting from
 491 the net vector sum of both remineralization, which increases both dPO_4^{3-} and dCo, and scavenging
 492 to Mn-oxides, which removes dCo in excess of dPO_4^{3-} from the water column (Noble et al., 2008;
 493 Hawco et al., 2017; Saito et al., 2017). The dCo vs. dPO_4^{3-} relationship observed on CICLOPS,
 494 however, displayed no such scavenging curl, indicating no clear signal of dCo loss due to
 495 scavenging, at least within timescales relevant to water column mixing. This finding is consistent
 496 with previous studies of the Ross Sea that have also observed little evidence of dCo loss via
 497 scavenging in the mesopelagic (Saito et al., 2010; Noble et al., 2013). The lack of a visible
 498 scavenging signal may be attributable to the deep winter mixed layers of coastal Antarctic seas
 499 that reach depths of up to 600 m and can extend to the seafloor (Smith and Jones 2015). This deep
 500 vertical mixing allows the dCo : dPO_4^{3-} ratio in the deep ocean to reset on an annual timescale,
 501 potentially erasing any signals of dCo scavenging, which would be expected to occur on a
 502 timescale of decades to centuries (Hawco et al., 2017). Additionally, Oldham et al. (2021)
 503 concluded that a suppressed Co scavenging flux might be the result of a unique Mn cycle in the
 504 Ross Sea, characterized by low to undetectable concentrations of Mn-oxide particles, slow rates
 505 of Mn-oxide formation, and the stabilization of organic dMn via Mn(III) ligands (Oldham et al.,
 506 2021).

507 The elevated dCo signal observed from several depths within 20 m of the seafloor were
 508 sourced from a benthic nepheloid layer: a near-seafloor region of the water column characterized
 509 by high particle abundance, turbulence, and isopycnal movement of both dissolved and particulate
 510 material along the seafloor (Gardner et al., 2018). The Ross Sea has been observed to display
 511 strong nepheloid layers as cold, dense water flows northward along the Ross Sea shelf until it
 512 reaches the shelf break, carrying suspended sediments with it along the seafloor (Budillon et al.,
 513 2006). Nepheloid layers tend to be enriched in dissolved trace metals like dFe, and can act as a
 514 source of micronutrients if upwelled to the surface ocean (Marsay et al., 2014; Noble et al., 2017).
 515 Elevated dCo concentrations within the Ross Sea nepheloid layer is a novel finding, as previous
 516 expeditions analyzing dCo concentrations in the Ross Sea did not sample as close to the seafloor



517 as the CICLOPS trace metal rosette was able to (Fitzwater et al., 2000; Saito et al., 2010; Noble et
 518 al., 2013). This finding is evidence of a dCo source to the deep ocean that may be upwelled to
 519 intermediate and upper ocean waters via vertical mixing.

520 4.2 Decreased Ross Sea dCo and labile dCo inventories

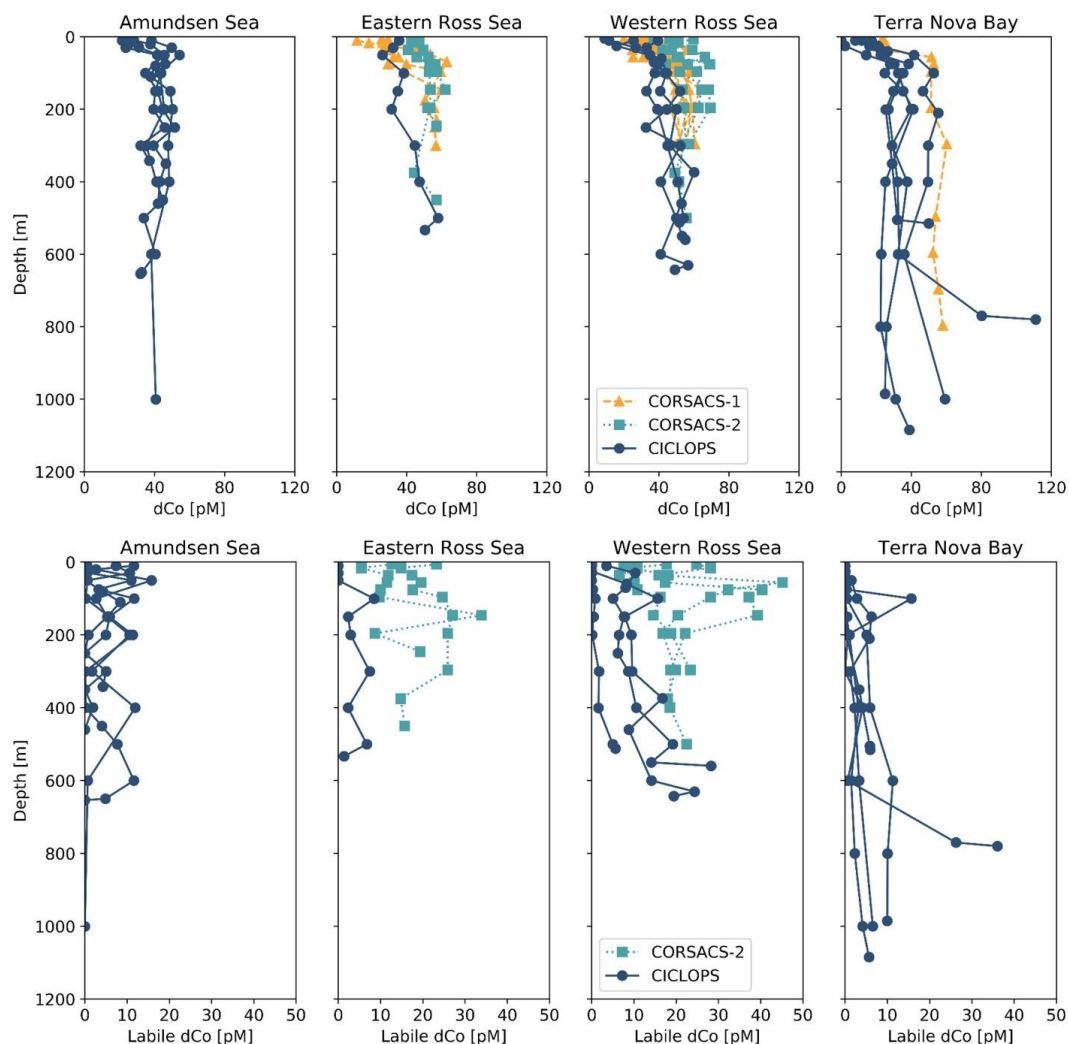
521 The dCo and labile dCo profiles observed along the 2017/2018 CICLOPS expedition
 522 displayed similar vertical structure as those observed along the 2005/2006 CORSACS expeditions;
 523 however, the CICLOPS dCo and labile dCo concentrations were notably lower throughout the
 524 water column compared to the CORSACS datasets (Fig. 8). This trend was particularly clear in
 525 the Ross Sea, where the stations from both expeditions contained the greatest regional overlap and
 526 labile dCo distributions from the prior 2006 CORSACS-2 expedition exceeded those observed on
 527 the 2017/2018 CICLOPS expedition (Fig. 9a-c; Table 4). The CORSACS-1 and CORSACS-2
 528 expeditions displayed average deep (≥ 100 m) dCo concentrations of 55 ± 4 pM and 56 ± 6 pM,
 529 respectively, and CORSACS-2 displayed average deep labile dCo concentrations of 21 ± 7 pM;
 530 on CICLOPS, in contrast, the Ross Sea displayed average deep dCo and labile dCo concentrations
 531 of 46 ± 8 pM and 9 ± 7 pM, respectively. Independent t-tests determined that CORSACS-1 and
 532 CORSACS-2 deep Ross Sea dCo values were statistically similar ($p = 0.27$) while deep CICLOPS
 533 dCo values were statistically different from CORSACS-1 and CORSACS-2 deep dCo ($p < 0.0001$;
 534 Table 4). This offset represents a mean dCo inventory loss of 8 – 10 pM dCo in the deep ocean,
 535 and approximately all of the difference can be accounted for by the loss of deep labile dCo (12 pM
 536 dCo; Fig. 9d-g), the more bioavailable form of dCo for biological uptake.

537 **Table 4.** The mean dCo and labile dCo observed in the deep (≥ 100 m) Ross Sea, and the average
 538 deep dCo loss between 3 previous sampling expeditions (CORSACS-1 in summer 2005/2006;
 539 CORSACS-2 in spring 2006; under-ice sampling in McMurdo Sound in spring 2009) and the
 540 CICLOPS expedition (2017/2018). Dissolved Co and labile dCo loss values were calculated as the
 541 difference between mean deep concentrations observed on previous expeditions and those
 542 observed on the CICLOPS expedition. No labile dCo data (n.d.) is presented from the CORSACS-
 543 1 expedition. Independent t-tests were performed to determine the significance of difference
 544 between the deep mean concentrations from previous expeditions compared to the CICLOPS
 545 expedition; * indicates a significant difference between CICLOPS and a previous expedition ($p <$
 546 0.005). The mean deep dCo concentrations from the CORSACS expeditions were not significantly
 547 different from each other ($p = 0.27$).

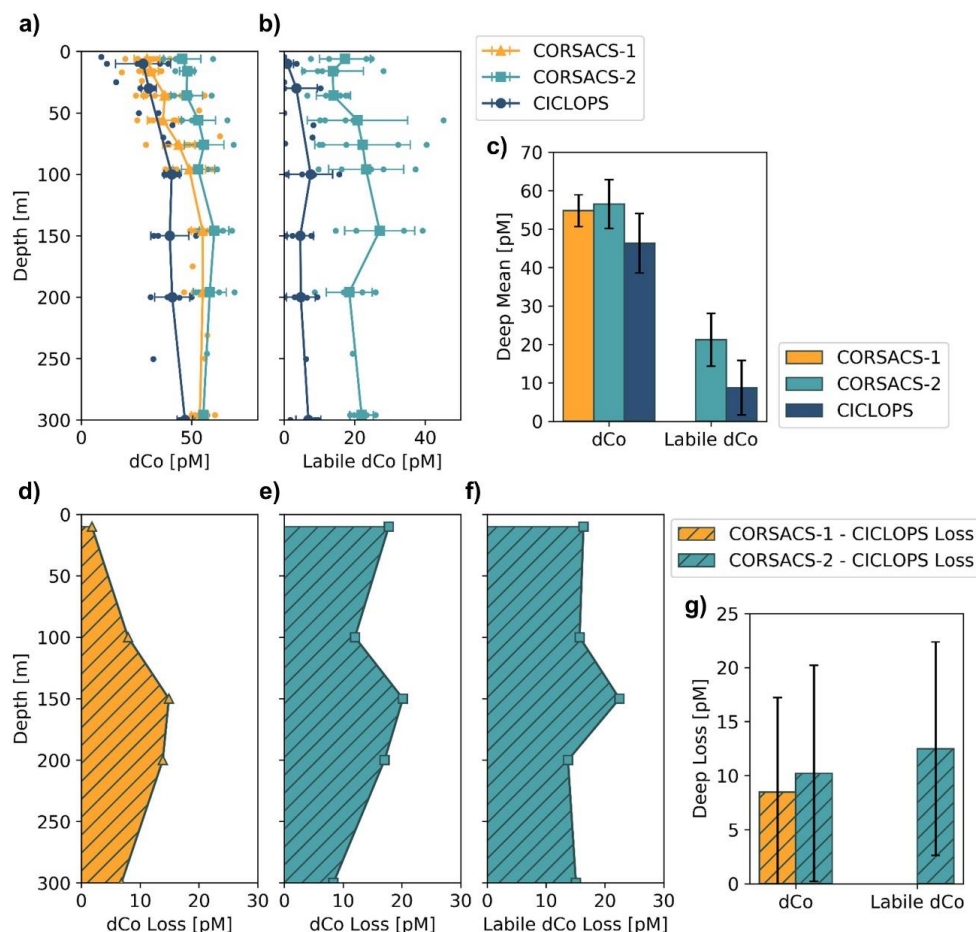
	dCo _{mean} [pM]	n	Labile dCo _{mean} [pM]	n	dCo Loss [pM]	p-value	Labile dCo Loss [pM]	p-value
CORSACS-1 ^a	55 ± 4	26	n.d.		8 ± 9	$< 0.0001^*$	--	--
CORSACS-2 ^a	56 ± 6	19	21 ± 7	20	10 ± 10	$< 0.0001^*$	12 ± 10	$< 0.0001^*$
McMurdo Sound ^b	51 ± 4	19	15 ± 2	19	4 ± 8	0.02	6 ± 7	0.0006*
CICLOPS	46 ± 8	32	9 ± 7	32	--	--	--	--

549 ^a Data originally published in Saito et al. (2010).

550 ^b Data originally published in Noble et al. (2013).



551
 552 **Figure 8.** Dissolved Co and labile dCo depth profiles from the CORSACS-1 (NBP0601;
 553 December 27, 2005 – January 23, 2006), CORSACS-2 (NBP0608; November 8, 2006 – December
 554 3, 2006) and CICLOPS (NBP-1801; December 11, 2017 – March 3, 2018) expeditions in the 4
 555 regions sampled by the CICLOPS expedition: Terra Nova Bay, the Western Ross Sea, the Eastern
 556 Ross Sea and the Amundsen Sea. The Eastern and Western Ross Sea stations are defined by being
 557 either east or west of the 175 °E longitudinal, respectively. The CORSACS expeditions did not
 558 extend to the Amundsen Sea, and no labile dCo was reported from the CORSACS-1 expedition.
 559 dCo data from the CORSACS expeditions was reported in Saito et al. (2010) and is accessible at
 560 <https://www.bco-dmo.org/dataset/3367>.



561
 562 **Figure 9.** Mean depth profiles of dCo (a) and labile dCo (b) from the Ross Sea from three sampling
 563 seasons, including the expeditions: CORSACS-1 (Summer 2005/2006), CORSACS-2 (Spring
 564 2006) and CICLOPS (Summer 2017/2018). Observed profile values are plotted as unconnected
 565 dots, and the mean profile is plotted for each depth at which at least three samples were analyzed.
 566 (c) The mean deep (≥ 100 m) dCo and labile dCo concentrations for stations in the Ross Sea on
 567 each expedition. The mean difference in the dCo (d, e) and labile dCo (f) profiles between the
 568 CORSACS and CICLOPS expeditions where sample depths were within 5 m of each other. (g)
 569 The mean deep (≥ 100 m) dCo and labile dCo concentration loss for stations in the Ross Sea. Error
 570 bars denote one standard deviation from the mean. No labile dCo data is available for the
 571 CORSACS-1 expedition. Mean values, loss values, and the results of independent t-tests to
 572 determine the significance of the deep dCo loss are given in Table 4.

573 In the near-surface (10 m), labile dCo was undetectable at 3 of the 4 stations in the Ross
 574 Sea on CICLOPS, and the near-surface labile : total dCo ratio in the one station where labile dCo
 575 was detectable (station 29; 3.5 pM labile dCo) was only 0.09. In contrast, the 2006 CORSACS-2
 576 expedition reported the presence of labile dCo at five stations with concentrations of 17 ± 7 pM at



577 6 m depth and 14 ± 9 pM at 16 m depth, and reported labile : total dCo ratios at 6 m and 16 m
578 depth of 0.37 ± 0.13 and 0.28 ± 0.17 , respectively. This trend can be at least partially explained by
579 the seasonality differences between the spring CORSACS-2 expedition and the summer CICLOPS
580 expedition; as the phytoplankton bloom progresses in the photic zone of the Ross Sea, labile dCo
581 concentrations would be drawn down by community uptake and would exhibit lower
582 concentrations later in the summer season. This seasonal trend was evident in the surface dCo
583 inventory differences between the summer CORSACS-1 and spring CORSACS-2 expeditions
584 (Fig. 9a,d,e). However, the low, often undetectable, labile dCo concentrations observed in the
585 surface Ross Sea on the CICLOPS expedition illustrate the intensity of bloom-driven labile dCo
586 depletion in the region, leaving 91–100% strong ligand-bound dCo in the surface Ross Sea. These
587 observations are consistent with the Co uptake rate measurements, which were found to be higher
588 on CICLOPS (0.84 pM d^{-1} , $n = 38$) compared to CORSACS-1 and CORSACS-2 (0.67 pM d^{-1} and
589 0.25 pM d^{-1} , respectively) (Saito et al., 2010; Rao, 2020).

590 Dissolved Co and labile dCo concentrations were also analyzed in the Ross Sea in 2009 by
591 sampling the water column below the McMurdo Sound seasonal sea ice in the early spring
592 (November 9–23) (Noble et al., 2013). Under the ice, the water column was well-mixed, and the
593 dCo and labile dCo profiles showed relative uniformity at all three stations measured (Fig. 2 of
594 Noble et al., 2013). In the deep ocean (≥ 100 m), the mean dCo and labile dCo concentrations
595 were 51 ± 4 and 15 ± 2 pM, respectively, which is lower than those observed on the 2005/2006
596 CORSACS expeditions and higher than those observed on the 2017/2018 CICLOPS expedition
597 (Table 4). The mean deep labile dCo concentrations from the McMurdo Sound fieldwork were also
598 significantly different from the mean deep labile dCo observed on CICLOPS ($p = 0.0006$),
599 displaying an average deep labile dCo difference of 6 pM. This dataset supports the possibility of
600 a long-term trend towards a decreasing deep dCo inventory in the Ross Sea, although the more
601 coastal location and difference in sea ice cover should be considered when comparing the
602 McMurdo Sound dataset to the CORSACS and CICLOPS observations. Notably, the methodology
603 and instrumentation used to measure both dCo and labile dCo on both CORSACS expeditions, the
604 McMurdo Sound fieldwork and the CICLOPS expedition were functionally identical, with the
605 exception of an autosampler (Metrohm 858 Sample Processor) used on the 2017/2018 CICLOPS
606 expedition.

607 The low labile dCo inventory in the Ross Sea was a surprising discovery during CICLOPS
608 since relatively high concentrations of labile dCo were previously noted to be a distinctive feature
609 of the Ross Sea and Southern Ocean when compared to the tropical and subtropical global oceans
610 (Saito et al., 2010). In prior studies in this region, high labile : total dCo ratios were hypothesized
611 to be due to the absence of ligand-producing – and vitamin B₁₂-producing – marine cyanobacteria
612 like *Synechococcus* in the Ross Sea (Caron et al., 2000; DiTullio et al., 2003; Bertrand et al., 2007),
613 since *Synechococcus*-dominated communities have been known to produce a substantial amount
614 of Co ligands (Saito et al., 2005). However, high Co ligand concentrations and low labile dCo
615 concentrations have previously been observed at a more pelagic location in the Southern Ocean
616 near New Zealand, where it was hypothesized that the decay of a eukaryotic phytoplankton bloom
617 generated higher abundances of Co-binding ligands in the surface ocean (Ellwood et al., 2005).

618 The decrease in the dCo and labile dCo inventories was apparent when the CICLOPS and
619 CORSACS dCo vs. dPO_4^{3-} relationships across all expedition regions were compared (Fig. 6c,e).
620 Over similar dPO_4^{3-} ranges, the CICLOPS dCo concentrations are generally lower than those
621 observed on CORSACS, and the CICLOPS labile dCo concentrations are considerably lower, with



622 labile dCo essentially absent from upper ocean samples with a dPO_4^{3-} concentration $< 1.75 \mu\text{M}$.
623 Despite the lack of observable scavenging, the CICLOPS dCo vs. dPO_4^{3-} relationship appeared to
624 be noticeably nonlinear throughout the water column ($R^2 = 0.42$), while CORSACS samples
625 displayed a more linear trend ($R^2 = 0.57$). The CICLOPS dCo vs. dPO_4^{3-} relationship creates a
626 concave, “scooped” shape where dCo was depleted relative to dPO_4^{3-} , displaying a lower slope in
627 the upper ocean than was observed on the CORSACS expeditions (Fig. 6c). This scooped shape
628 was particularly evident in Terra Nova Bay where the upper ocean dCo : dPO_4^{3-} stoichiometric
629 slope was the lowest ($26 \pm 4 \mu\text{mol} : \text{mol}$; $R^2 = 0.65$). The depletion of dCo relative to dPO_4^{3-}
630 observed on CICLOPS appears driven by the shift in Co speciation as a result of near-total uptake
631 of the upper ocean labile dCo fraction and subsequent dominance of the remaining strong ligand-
632 bound dCo fraction in the upper ocean. Similar to the deep dCo loss described above, the difference
633 between the CORSACS and CICLOPS dCo vs. dPO_4^{3-} relationship can be accounted for by the
634 depletion of the labile dCo inventory. In the deep ocean where both dCo and dPO_4^{3-} are more
635 abundant, the large range in dCo concentrations relative to dPO_4^{3-} concentrations may be evidence
636 of deep inputs of dCo and labile dCo from the nepheloid layer, which was more attentively sampled
637 on CICLOPS than either CORSACS expedition (Sect. 4.1).

638 4.3 Dissolved Co, Zn and Cd stoichiometry

639 Dissolved Zn concentrations observed on CICLOPS were low in the surface ocean,
640 particularly in Terra Nova Bay, where dZn concentrations in the sub-nanomolar ranges were
641 observed (average dZn = 0.87 ± 0.42 at 10 m depth, $n = 11$). Marine microbes require Zn for a
642 wide range of metabolic uses; for example, eukaryotic phytoplankton use Zn as a cofactor in
643 carbonic anhydrase (Roberts et al., 1997; Morel et al., 2020) and bacteria such as
644 *Pseudoalteromonas* use Zn in a range of proteases (Mazzotta et al., 2021). Prior culture studies
645 have found that Zn scarcity can lead to co-limitation of both Zn and carbon in several eukaryotic
646 phytoplankton strains (Morel et al., 1994; Sunda and Huntsman, 2000), and field incubation
647 experiments have shown evidence for Zn co-limitation with Fe (Jakuba et al., 2012) and silicate
648 (Chappell et al., 2016) in the Pacific Ocean. During the CICLOPS expedition, an incubation
649 experiment performed at Station 27 in Terra Nova Bay found compelling evidence for Zn and Fe
650 co-limitation, which constrained Chl-a production and DIC draw-down by phytoplankton in the
651 region (Kellogg et al., [Submitted]).

652 Many but not all phytoplankton are able to substitute Co and Cd for Zn as their carbonic
653 anhydrase metallic cofactor (Lee and Morel, 1995; Sunda and Huntsman, 1995; Lane et al., 2005;
654 Kellogg et al., 2022), which provides metabolic flexibility and a competitive edge in low-dZn
655 environments (Kellogg et al., 2020). The Cd-containing carbonic anhydrase CDCA is currently
656 the only known metabolic use of Cd, and the uptake of dCd and dCo in the photic zone, both metals
657 which are typically less abundant than dZn in the oceans, often increases under low dZn conditions
658 (Sunda and Huntsman, 1995, 1996; Jakuba et al., 2008; Kellogg et al., 2020; Morel et al., 2020).
659 Cations like Zn, Cd and Co that possess similar charge and atomic radii often share the same
660 transporter uptake systems, and the relative availability of different metal cofactors for use in an
661 organism’s metalloproteome is partially determined by the environmental metal concentrations
662 and the affinity of the metals for ligands associated with a cell’s metal transport proteins (Irving
663 and Williams, 1948; Sunda and Huntsman, 1992, 1995). When dZn concentrations are low, more
664 Cd and Co are able to bind to the transporter ligands despite the relative stability of their ligand-
665 bound complexes, which tend to be lower for Co than for Zn. Through this mechanism, dZn



666 concentrations and cycling can influence the distribution and uptake of Co and Cd, particularly in
667 low dZn environments like the Ross Sea and Terra Nova Bay.

668 The dZn vs. dPO_4^{3-} and dCd vs. dPO_4^{3-} relationships observed in the Amundsen Sea, Ross
669 Sea and Terra Nova Bay were compared relative to dCo vs. dPO_4^{3-} (Fig. 7; Table 3). The resulting
670 shapes of these relationships were similar to that of dCo vs. dPO_4^{3-} , exhibiting distinct differences
671 in slope between surface and deep waters. The stark difference in trace metal stoichiometry slopes
672 between the upper and deep ocean is likely driven by differences in metal speciation over depth.
673 In the surface ocean, a shallower trace metal : dPO_4^{3-} slope suggests a trace metal fraction that is
674 largely bound to strong organic ligands, with a smaller excess labile fraction. The more
675 bioavailable labile fraction of metals would have been drawn down by phytoplankton, whose
676 uptake transport systems preferentially bind to labile metals. At deeper depths, the presence of
677 labile metals in excess of strong organic ligands results in a higher metal : dPO_4^{3-} slope. For this
678 analysis, the depth threshold that separates the upper ocean from the deep ocean was selected
679 manually in order to optimize the linear fit of the upper and deep ocean trends and to best capture
680 the depth dependence of the observed trace metal stoichiometries. This depth threshold can best
681 be conceptualized as an inflection point that represents the largest change in trace metal
682 concentrations with respect to depth or, in this case, dPO_4^{3-} concentration. The depth threshold
683 used for dCo in both the Ross Sea and Terra Nova Bay (100 m) is deeper than those used for dZn
684 and dCd, (range of 25 – 50 m). Thus, the inflection points of the “scoops” in the trace metal
685 stoichiometries are driven by the uptake stoichiometry of the region’s phytoplankton community
686 rather than the mixed layer depth of the upper ocean.

687 A shallow dCo : dPO_4^{3-} slope that extends below the photic zone could suggest Co uptake
688 by heterotrophic bacteria, archaea and possibly sinking phytoplankton below the photic zone.
689 Heterotrophic prokaryotic uptake of labile Co is largely driven by the bacteria and archaea that
690 contain a vitamin B₁₂ synthesis pathway that is absent in all eukaryotes (Warren et al., 2002;
691 Osman et al., 2021); unlike carbonic anhydrase, the use of Co as a co-factor in the vitamin B₁₂
692 corrin ring structure cannot be substituted for by other divalent cations like Zn and Cd. Many
693 vitamin B₁₂-synthesizing bacteria possess genes for Co(II)-specific transporters in addition to more
694 general metal ion transporters, and the Co-specific transporters are regulated by cellular
695 concentrations of vitamin B₁₂, illustrating the importance of vitamin B₁₂ synthesis in driving
696 bacterial Co uptake (Osman et al., 2021); however, this mechanism has not been observed within
697 marine bacterial communities. Additionally, vitamin B₁₂ uptake by both prokaryotes and
698 eukaryotes has been found to be common in Antarctic coastal communities (Taylor and Sullivan,
699 2008; Rao, 2020), and likely contributes to the depletion of ligand-bound dCo in both the surface
700 and mesopelagic ocean.

701 The shallower Zn apparent nutricline could also be explained by the higher stability of Zn
702 metal-ligand complexes compared to Co complexes within phytoplankton metabolisms, allowing
703 higher uptake rates of dZn when available (Irving and Williams, 1948; Sunda and Huntsman,
704 1995). The vertical dimension of trace metal loss captured by a comparison of these apparent
705 nutriclines could be conceptualized as a time-dependent process driven by the phytoplankton
706 community’s preference for each trace metal, with preferred nutrients like Zn exhibiting a
707 shallower stoichiometric inflection point arising from the rapid depletion of the metal within the
708 photic zone, and nutrients like dCo, which is often taken up by eukaryotes when dZn is scarce
709 (Sunda and Huntsman, 1995; Kellogg et al., 2020), exhibiting a deeper stoichiometric inflection
710 point below the photic zone. This analysis suggests that substitution at the interface of the uptake



711 mechanism for trace metal transporters at least partially controlled the stoichiometry of Zn/Cd/Co
712 distributions and uptake in the upper ocean.

713 4.4 Zn/Cd/Co uptake using a shared trace metal membrane transport system

714 This study synthesized dissolved concentration and uptake datasets for Co, Zn and Cd
715 (Table 5), three trace metal nutrients whose use by phytoplankton is collectively integral to surface
716 ocean productivity and the biogeochemical cycling of Fe, vitamin B₁₂ and carbon in the Southern
717 Ocean. This combined dataset is ideal for interrogating questions of environmental competitive
718 inhibition of Zn, Cd and Co transport in low-dZn environments. The observation of order of
719 magnitude trends in trace metal uptake rates over depth profiles ($\rho\text{Zn} > \rho\text{Cd} > \rho\text{Co}$) was novel,
720 and paralleled the order of magnitude trends of trace metal concentrations in seawater ($[\text{Zn}] > [\text{Cd}]$
721 $> [\text{Co}]$; Fig 5). This environmental observation reflected the findings of numerous culture
722 experiments that quantify the uptake of trace metals as a function of the concentration of available
723 labile metals and the affinity of the metal for a cell transporter's binding ligand (Irving and
724 Williams, 1948; Sunda and Huntsman, 1992, 1995, 2000; Kellogg et al., 2020).

725 **Table 5.** Dissolved stoichiometric ratios and uptake stoichiometric ratios of five station profiles
726 for Co, Cd and Zn. The $d\text{Co} : d\text{Cd} : d\text{Zn} : d\text{PO}_4^{3-}$ ratio is the dissolved stoichiometry of metals
727 present in the water column normalized to $d\text{PO}_4^{3-}$, and the $\rho\text{Co} : \rho\text{Cd} : \rho\text{Zn}$ ratio is the uptake
728 stoichiometry of microbial communities normalized to ρCo .

Region	Station	Depth [m]	$d\text{Co} : d\text{Cd} : d\text{Zn} : d\text{PO}_4^{3-}$	$\rho\text{Co} : \rho\text{Cd} : \rho\text{Zn}$
Amundsen Sea	4	10	19 : 314 : 1,716 : 1,000,000	1 : 8 : 56
		30	23 : 295 : 1,889 : 1,000,000	1 : 16 : 88
		50	24 : 293 : 2,096 : 1,000,000	1 : 15 : 108
	11	10	13 : 204 : 1,018 : 1,000,000	1 : 10 : 77
		20	15 : 212 : 970 : 1,000,000	1 : 13 : 89
		30	17 : 231 : 1,290 : 1,000,000	1 : 29 : 294
		50	19 : 280 : 1,835 : 1,000,000	1 : 0* : 229
		75	21 : 301 : 2,009 : 1,000,000	1 : 0* : 532
		100	23 : 358 : 2,727 : 1,000,000	1 : 11 : 708
		150	17 : 313 : 1,974 : 1,000,000	1 : 0* : 797
200	17 : 325 : 2,137 : 1,000,000	1 : 3 : 885		
Ross Sea	20	30	17 : 323 : 1,846 : 1,000,000	1 : 13 : 349
		50	13 : 305 : 2,020 : 1,000,000	1 : 11 : 163
		100	17 : 333 : 2,400 : 1,000,000	1 : 0* : 376
		150	16 : 330 : 2,321 : 1,000,000	1 : 0* : 507
		200	14 : 336 : 2,358 : 1,000,000	1 : 0* : 913
Terra Nova Bay	22	10	15 : 136 : 617 : 1,000,000	1 : 12 : 81
		25	10 : 158 : 546 : 1,000,000	1 : 11 : 75
		40	11 : 254 : 1,127 : 1,000,000	1 : 29 : 166
		75	13 : 301 : 1,965 : 1,000,000	1 : 7 : 228
		100	11 : 304 : 1,938 : 1,000,000	1 : 56 : 705
		150	16 : 310 : 2,212 : 1,000,000	1 : 122 : 584
	57	50	13 : 179 : 894 : 1,000,000	1 : 17 : 37
		75	13 : 297 : 1,644 : 1,000,000	1 : 3 : 18
		100	15 : 320 : 1,798 : 1,000,000	1 : 8 : 40

729

730

*Denotes depths at which ρCd was under the methodological detection limit.



731 Evidence for elevated Co uptake in the low-dZn environments of the surface ocean were
 732 supported by the trace metal uptake rates. When ρZn and ρCd was normalized to ρCo ($\rho\text{TM} : \rho\text{Co}$;
 733 Fig. 5), deviations from these order-of-magnitude trends were observed; in particular, at Stations
 734 4 and 11 in the Amundsen Sea and Station 22 in Terra Nova Bay, ρZn and ρCd stoichiometry
 735 relative to ρCo tended to decrease towards the surface in the upper 50 m, while the opposite trend
 736 appeared to occur at Station 57 in the late summer. The surface-most trends of stations 20 and 57
 737 were undetermined due to a lack of a 10 m ρCo value. This increasing surface Co uptake
 738 stoichiometry relative to Zn and Cd at Stations 4, 11 and 22 – stations that also displayed
 739 significant phytoplankton blooms – suggests that Co uptake increased in low-Zn environments,
 740 while later in the summer at Station 57, ρCo lessened relative to ρZn , possibly due to the deepening
 741 of the mixed layer in February, bringing additional dZn to the upper ocean via vertical mixing
 742 (Fig. 4). The increase in the observed ρCo rate was likely due to the upregulation of the shared Zn
 743 and Co uptake transporter system.

744 From laboratory culture experiments aimed at examining the microbial uptake of Zn and
 745 other trace metals, it is apparent that many diatoms and coccolithophores contain two distinct Zn
 746 uptake systems: a low-affinity system that operates at higher concentrations of dZn and a high-
 747 affinity system that functions at lower concentrations of dZn (Sunda and Huntsman, 1992; John et
 748 al., 2007). Both transport mechanisms are relatively unspecific as to the divalent metals transported
 749 into the cell; the low-affinity system is known to transport Zn, Cd and Mn, while the high-affinity
 750 system transports Zn, Cd and Co. (Sunda and Huntsman, 1995, 1996); thus, Co uptake is often
 751 inhibited at high dZn concentrations when the low-affinity system is active (Sunda and Huntsman,
 752 1995; Sunda 2012). In culture, diatoms have been observed to switch from the low-affinity to the
 753 high-affinity transport system between $10^{-10.5}$ and $10^{-9.5}$ M dZn^{2+} (Sunda and Huntsman, 1992;
 754 John et al., 2007), a relevant range for the lowest values of total dZn observed in the surface ocean
 755 on CICLOPS (dZn minimum = 1×10^{-10} M at Station 46, 10 m depth), and the dZn^{2+} pool would
 756 have been even smaller due to organic complexation.

757 To investigate the influence of transporter competitive inhibition on trace metal uptake via
 758 the high-affinity uptake system, we can estimate the predicted ρCo , ρCd and ρZn values given the
 759 observed trace metal concentrations with an equation adapted from Michaelis-Menten enzyme-
 760 substrate kinetics (Sunda and Huntsman, 1996, 2000):

$$761 \quad \text{Predicted } \rho M = \frac{V_{\max}[M^{2+}]K_M}{[Co^{2+}]K_{Co} + [Cd^{2+}]K_{Cd} + [Zn^{2+}]K_{Zn}}$$

762 where M is the trace metal (Co, Cd, Zn) whose uptake is being calculated, V_{\max} is the saturation
 763 uptake rate of the transporter system, and K_{Co} , K_{Cd} and K_{Zn} are steady state affinity constants for
 764 the metal-ligand complex associated with the membrane transporter. For this system, we assumed
 765 $K_{Zn} = K_{Cd} = K_{Co} = 10^{9.6}$, where $10^{9.6}$ is the value of K_{Zn} for the high-affinity uptake system
 766 determined by Sunda et al. (1992), and that 99% of the dCo, dCd and dZn inventory was bound to
 767 strong organic ligands, leaving 1% of the total metal concentration labile. Note that the assumption
 768 that K and the percent labile multipliers are equal for all metals results in their value being nullified
 769 by their presence in both the numerator and denominator of the predicted uptake equation, and so
 770 their assumed values have no numerical impact on the predicted uptake values. It was also assumed
 771 that V_{\max} values for each trace metal were equal, which is likely a reasonable assumption for metals
 772 that share an uptake system, although V_{\max} is known to vary with trace metal concentration, a
 773 function that we have assumed here to be negligible (Sunda and Huntsman, 1985, 1996; Sunda,



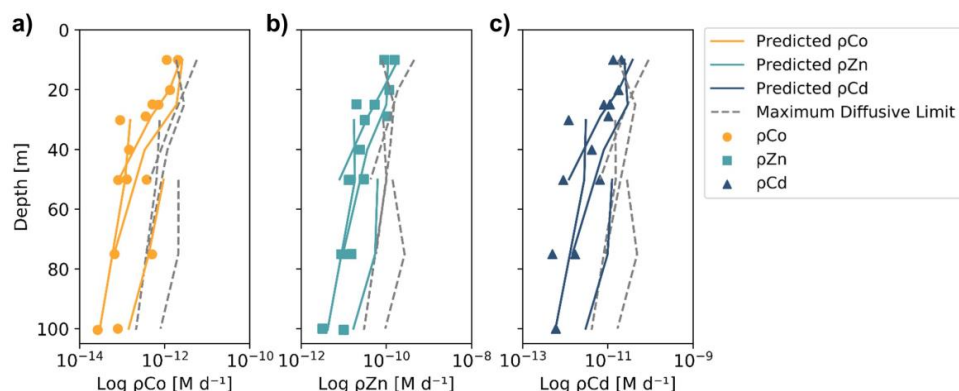
774 1989). V_{\max} is in units of $\mu\text{mol} (\text{mol C})^{-1} \text{d}^{-1}$, and the predicted trace metal uptake rates were
775 converted to units of M d^{-1} using a C : Chl-a ratio of 130 w/w, derived from the Ross Sea
776 phytoplankton community (DiTullio and Smith, 1996).

777 When the predicted metal uptake rates were calculated using a V_{\max} value of 262 $\mu\text{mol} (\text{mol}$
778 $\text{C})^{-1} \text{d}^{-1}$ from previous Zn culturing experiments (Sunda and Huntsman, 1992), the resulting values
779 recreated the trend of the observed trace metal uptake profiles, with higher uptake rates in the
780 surface ocean and lower rates below the photic zone, but the predicted values were over an order
781 of magnitude greater than the measured uptake rates (Fig. A1). This offset may be due to several
782 factors: (1) the assumed C : Chl-a ratio to scale predicted uptake with observed biomass may be
783 high, (2) the V_{\max} value calculated from laboratory experiments may be high, or (3) the
784 assumptions that the speciation of the dissolved trace metals are 99% strongly-bound at all depths,
785 for all metals is incorrect. The final explanation may play a role in the offset between the predicted
786 and observed uptake rates, and illustrates the complexities of translating lab-based culture work to
787 environmental measurements and in-situ analyses. The V_{\max} value is also relatively unconstrained,
788 and it is reasonable to assume it may be lower in the Ross Sea than observed in culture if the
789 phytoplankton exhibit suppressed metal quotas to survive in a metal-deplete environment. With
790 this in mind, the V_{\max} value was tuned to 4 $\mu\text{mol} (\text{mol C})^{-1} \text{d}^{-1}$ to fit the observed uptake rates,
791 which is lower than any Co, Cd or Zn V_{\max} reported in the literature from culture studies (Fig. 10).
792 Using the tuned V_{\max} value, the high-affinity uptake system equation properly predicts the order
793 of magnitude trends inherent in the observed Co/Cd/Zn uptake rates. This analysis demonstrates
794 the measured uptake rates from the Ross Sea were likely driven by the concentration ratios of
795 available metals throughout the water column, following a high-affinity transporter model of Co,
796 Cd and Zn uptake.

797 The maximum diffusive limit, a calculation of the phytoplankton community's maximum
798 diffusion rate for the uptake of trace metal nutrients through their cell membranes, was also
799 estimated and compared to the observed and predicted uptake rate profiles. The physical limits of
800 uptake via diffusion was determined as a function of the surface area of phytoplankton membranes
801 (Sunda and Huntsman, 1992):

802
$$\text{Maximum diffusive limit} = 4\pi rD[M^{2+}]$$

803 where r is the equivalent spherical radius of a phytoplankton cell, assumed to be 3 μm , a reasonable
804 value for diatom species, and D is a diffusion rate constant of $2 \times 10^{-6} \text{cm}^2 \text{s}^{-1}$, calculated for Zn^{2+}
805 at 20°C (Sunda and Huntsman, 1992). The diffusive limit was converted to units of M d^{-1} using a
806 C : cell volume ratio of 12.5mol C L^{-1} , which is the average of two diatom ratios reported in Sunda
807 and Huntsman (1995) (11 and 14mol C L^{-1}), and the same C : Chl-a ratio of 130 w/w used for the
808 predicted uptake rate estimate above (DiTullio and Smith, 1996). The resulting diffusive limit
809 profiles are highly dependent on the assumed speciation of each trace metal; when the dCo, dCd
810 and dZn inventories were assumed to be 99% bound (Fig. 10), the maximum diffusive limit was
811 slightly greater than the predicted and observed uptake rates, but when the inventories were
812 assumed to be 100% labile (Fig. A1), the diffusive limit greatly exceeded the uptake rates by
813 several orders of magnitude. Since the metal inventories almost certainly vary in their speciation
814 of dZn and dCd over depth, as was observed in the dCo inventory, an accurate maximum diffusive
815 limit would exist between the two extremes of 0% bound and 99% bound, and might be expected
816 to be greater at deeper depths, where a higher fraction of the dissolved metal inventory is labile.
817 For additional analysis of the predicted metal uptake ratios and the maximum diffusive limit, see
818 Appendix H.



819

820

821

822

823

824

825

Figure 10. Observed (markers) and predicted (solid lines) trace metal uptake rate (ρ) profiles for Co (a) Zn (b) and Cd (c) from Stations 11, 20, 22 and 57. The maximum diffusive limit profiles (dashed lines) are shown as an estimate of the physical limits of metal diffusion through uptake transporters. The predicted uptake rates were tuned to best fit the observed uptake rate trends by using a V_{\max} value of $4 \mu\text{mol} (\text{mol C}^{-1}) \text{d}^{-1}$, and the maximum diffusion limit estimation assumed a speciation of 0.01% labile metals.

826

4.5 Vitamin B₁₂ and Zn stress, and their implications for increasing biological dCo demand

827

828

829

830

831

832

833

834

835

836

837

838

839

840

841

842

The near-absence of labile dCo and low concentration of ligand-bound dCo in coastal Antarctic seas may indicate a larger shift in the region towards vitamin B₁₂ limitation. Vitamin B₁₂ has been shown to be co-limiting with Fe in the Ross Sea and elsewhere (Sañudo-Wilhelmy et al., 2006; Bertrand et al., 2007), and increased vitamin B₁₂ uptake by both bacterioplankton and eukaryotic phytoplankton has been observed in incubation experiments following the alleviation of surface ocean Fe limitation (Bertrand et al., 2011). Two primary sources of Fe to the Antarctic seas are a flux of lithogenic Fe from melting ice shelves along the continent and sediment resuspension along the seafloor, both of which have been observed to be meaningful Fe sources to the Amundsen Sea (Planquette et al., 2013; St-Laurent et al., 2017). The source of particulate Fe from glacial meltwater to coastal Antarctic seas has been increasing over the past several decades and is expected to continue to increase as Antarctic ice shelves and glaciers melt and retreat due to global climate change (Monien et al., 2017). The source of particulate Co from glacial meltwater would also be expected to increase since Co, like Fe, has been observed to be transported from the Antarctic continent via ice melt (Westerlund and Öhman, 1991), and it is unclear what role this presumably increasing source of Co to the surface ocean plays in the reduced inventories of dCo in the surface ocean.

843

844

845

846

847

848

849

850

851

Although it is difficult to definitively conclude that the low dCo inventory observed on CICLOPS is representative of a decadal trend towards vitamin B₁₂ limitation and not simply variation in micronutrient availability and community structure, the inventory and stoichiometric uptake trends documented in this study are compelling evidence for a changing biogeochemical Co cycle in the coastal Southern Ocean. Paired with the recent discovery of Zn/Fe co-limitation in Terra Nova Bay (Kellogg et al., [Submitted]), these results suggest a complex landscape of micronutrient scarcity and limitation in coastal Antarctic seas where plankton community structures and Fe additions from melting ice sheets can generate patches of vitamin B₁₂ and Zn limitation within a broadly Fe-scarce HNLC region.



852 The bacterial community is essential to the development and alleviation of vitamin B₁₂
853 limitation within a eukaryotic phytoplankton bloom since only prokaryotes possess the metabolic
854 pathway to synthesize the vitamin (Warren et al., 2002; Croft et al., 2005). In the Southern Ocean,
855 near-zero counts of photosynthetic bacteria indicate that the heterotrophic bacterial communities
856 are primarily responsible for vitamin B₁₂ production in the region (Bertrand et al., 2011). Vitamin
857 B₁₂ can become limiting when the bacterial community is low in abundance and/or growth limited
858 by a different nutrient such as dissolved organic matter (DOM). In the Ross Sea, bacterioplankton
859 have been found to be growth limited by an inadequate supply of DOM (Church et al., 2000;
860 Bertrand et al., 2011), and there can be up to a one-month lag between the onset of the spring
861 phytoplankton bloom and an associated bacterial bloom stimulated by phytoplankton DOM
862 production (Ducklow et al., 2001). This offset suggests that vitamin B₁₂ limitation among
863 eukaryotes is most probable earlier in the season within the spring bloom. Additionally, low
864 abundances of mesozooplankton and microzooplankton grazing rates in the Ross Sea create
865 phytoplankton blooms with low grazing pressure (Caron et al., 2000; Ducklow et al., 2001), which
866 may allow low DOM conditions to persist later into a bloom and exacerbate vitamin B₁₂ stress
867 among eukaryotes.

868 A shift towards vitamin B₁₂ limitation would likely favor phytoplankton with flexible
869 metabolisms that are able to reduce their demand for Co and vitamin B₁₂ when necessary.
870 Organisms that can express the vitamin B₁₂-independent *metE* gene may out-compete those
871 expressing the vitamin B₁₂-dependent *metH* gene (Rao et al., [In review]; Rodionov et al., 2003;
872 Bertrand et al., 2013; Helliwell 2017). *P. antarctica*, for example, may be well suited to periods
873 of vitamin B₁₂ limitation due to the symbiotic bacterial microbiomes that form within its colonies
874 and produce B vitamins that allow the colonies to grow when B vitamins are otherwise unavailable
875 (Brisbin et al., 2022). *P. antarctica* has also been found to express a novel *metE*-fusion gene when
876 vitamin B₁₂ limited and *metH* gene while vitamin-replete, suggesting a highly flexible vitamin B₁₂
877 metabolism (Rao et al., [In review]).

878 There is compelling evidence for high rates of biological Co uptake in the Ross Sea during
879 the 2017/2018 summer compared to the 2005/2006 summer driven by the uptake of dCo from
880 vitamin B₁₂ and Zn scarcity. Together, these two stressors increase the rate of Co uptake as well
881 as the Co : C stoichiometry of phytoplankton biomass. The stoichiometry of Co uptake has been
882 observed to be highly plastic in this study and others, responding to the availability of other
883 micronutrients and the requirements of the microbial community (Sunda and Huntsman, 1995;
884 Saito et al., 2017). An increase in ρCo could then result in a decrease of the Co inventory in coastal
885 Antarctic seas, following the mechanism detailed below.

886 Biological uptake alone would not permanently remove Co from the water column; uptake
887 only shifts Co from the dissolved phase to the particulate phase, where POM remineralization
888 restores Co back to the dissolved phase. The net removal pathways of Co include (1) burial as
889 POM, (2) particle scavenging and (3) depletion of dCo into Circumpolar Deep Water (CDW) and
890 Antarctic Bottom Water (ABW). We have already noted that Co scavenging to Mn-oxides is
891 particularly low in the Southern Ocean (Oldham et al., 2021). The advection of dCo into CDW
892 may not be at a steady state throughout the year since cycles of ice melt and formation affect the
893 mixing of CDW and formation of dense Antarctic Bottom Water (ABW), and so may represent a
894 removal pathway for dCo on an annual cycle. However, an increase in the burial flux of Co in
895 POM is the most likely pathway for sustained loss of the Co inventory. When the ρCo rate
896 increases, the stoichiometry of Co incorporation into biomass relative to P would also increase.



897 Over the years, a strengthened demand for Co via vitamin B₁₂ and Zn stress could result in a steady
 898 loss of Co if the Co : C and Co : PO₄³⁻ stoichiometry of POM increases but the remineralization of
 899 POM is unchanged, increasing the flux of particulate Co into the deep ocean and sediments. In the
 900 winter, sea ice covers the Antarctic seas and the water column mixes, a process that would
 901 propagate the low dCo concentrations from the photic zone into the deep ocean and result in a
 902 steady loss of the dCo inventory throughout the water column.

903 Additionally, warming surface ocean temperatures likely play a role in phytoplankton
 904 productivity and nutrient uptake. Increasing both dFe availability and temperature have been
 905 shown to significantly increase phytoplankton growth and phytoplankton abundance in the Ross
 906 Sea, and impact community structure (Rose et al., 2009; Spackeen et al., 2018; Zhu et al., 2016).
 907 From a kinetic perspective, higher surface temperatures would be expected to increase the uptake
 908 rates of nutrients, including micronutrients like Fe, Co and Zn, by increasing the value of *K_M*.
 909 However, the effects of temperature on productivity and community composition are more
 910 complex since increasing ocean temperatures would also decrease the solubility of CO₂, change
 911 the seasonality of ice cover and thus sunlight availability, and affect water column turnover and
 912 mixing regimes (Rose et al., 2009). The effects of warming temperatures on the intricate landscape
 913 of nutrient availability and limitation regimes described here is an open question in this study.

914 4.6 A two-box model that describes a mechanism for deep dCo inventory loss

915 To test the proposed mechanism that higher Co uptake rates and winter mixing can lead to
 916 a deep inventory loss of ~10 pM Co over 12 years, a time step two-box model of a 1 m² water
 917 column was created in Microsoft Excel to simulate the Ross Sea dCo cycle. A schematic of the
 918 modeled dCo cycle is presented in Fig. 11, flux equations to describe the biogeochemical cycling
 919 of Co are presented in Appendix I, and the parameters used to simulate dCo loss over 12 years and
 920 a hypothetical steady state condition are given in Table 6.

921 The change in dCo concentration over time ($d[dCo]/dt$) for a surface ocean (0–100 m) and
 922 deep ocean (100–500 m) was calculated as the sum of the dCo source fluxes minus the sum of the
 923 sink fluxes:

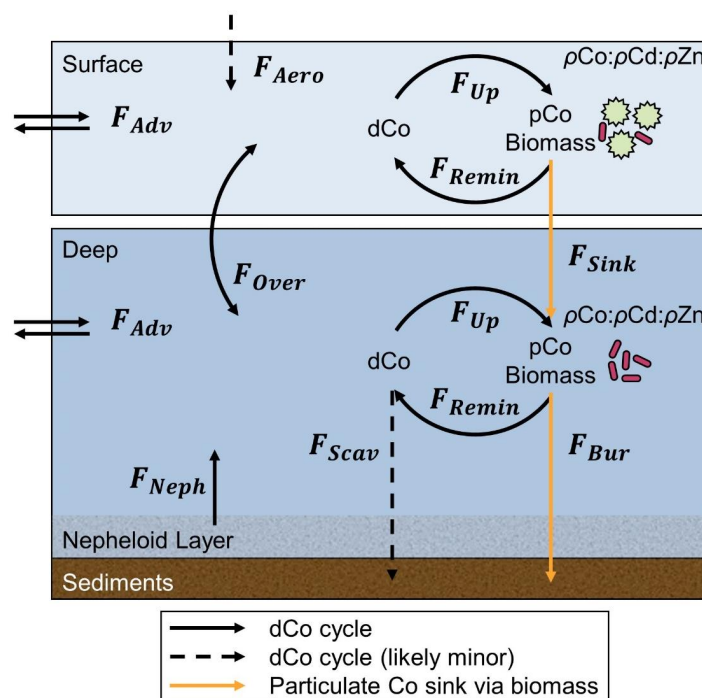
$$924 \quad \left(\frac{d[dCo]}{dt}\right)_{Surface} = \frac{F_{Over} + F_{Remin} - F_{Up}}{V_{Surface}}$$

$$925 \quad \left(\frac{d[dCo]}{dt}\right)_{Deep} = \frac{F_{Remin} + F_{Neph} - F_{Up} - F_{Over}}{V_{Deep}}$$

926 where *F_{Over}* is the overturning flux between the two boxes, *F_{Remin}* is the remineralization flux, *F_{Up}*
 927 is the biological uptake flux, and *F_{Neph}* is the flux of dCo from the nepheloid layer into the deep
 928 ocean (Table B1). *F_{Up}* was calculated using the measured ρCo uptake rates observed on the
 929 CORSACS and CICLOPS expeditions, and *F_{Remin}* was calculated using an assumed surface and
 930 deep remineralization factor (RF) of 0.9, indicating that 90% of the POM generated in the surface
 931 ocean is remineralized back to its inorganic dissolved components. In the Southern Ocean, the
 932 fluxes of scavenging and aerosol deposition would be relatively negligible, so these fluxes have
 933 been omitted from the model. The magnitude of *F_{Neph}* in the Ross Sea remains unconstrained, and
 934 in this model, the deep nepheloid dCo source was used as an adjustable parameter to tune the
 935 magnitude of deep dCo loss to be 10 pM over 12 years, which represents the approximate observed
 936 differences between the CORSACS and CICLOPS expeditions detailed in Sect. 4.2. A *F_{Neph}* was



937 calculated to be $3550 \text{ pmol m}^{-2} \text{ d}^{-1}$ to the deep ocean, but this should not be considered a
 938 meaningful calculation of the observed nepheloid layer flux.



939 **Figure 11.** A schematic of the dCo cycle (black) and select processes of the particulate Co (pCo)
 940 cycle (orange) presented as a simplified two-box model. Net fluxes of the dCo cycle include
 941 sources from aerosol deposition (F_{Aero}), bottom sediments and the nepheloid layer (F_{Neph}), and
 942 scavenging to Mn-oxides particles (F_{Scav}) which likely represents a minor flux in the coastal
 943 Antarctic seas. Internal cycling fluxes include horizontal advection (F_{Adv}), water column
 944 overturning or mixing (F_{Over}), biological uptake (F_{Up}) and remineralization of pCo (F_{Remin}). Fluxes
 945 of pCo shown here include sinking biomass from the surface into the deep ocean (F_{Sink}) and pCo
 946 burial into sediments along the seafloor (F_{Bur}). The biological uptake of dCo is influenced by the
 947 relative stoichiometric uptake of Co, Zn and Cd ($\rho_{Co} : \rho_{Cd} : \rho_{Zn}$) among the microbial
 948 community. Differential equations that describe and quantify these fluxes are presented in
 949 Appendix I.
 950

951 In the Ross Sea, the deep winter mixed layer can extend 600 m to the seafloor and turn
 952 over the whole water column in some locations (Smith and Jones, 2015), mixing the surface and
 953 deep ocean under the winter sea ice and resulting in near-vertical profiles of dCo in the early spring
 954 (Noble et al., 2013). Here, the winter mixing process was modeled by combining the surface and
 955 deep ocean boxes into one homogenized box during the winter season (151 days, ~5 months). The
 956 dCo concentrations of the winter box were calculated using a volume-weighted average (see
 957 Appendix I).

958 **Table 6.** Parameters of the Co cycle two-box model, run as both a steady state model with lower
 959 Co uptake rates (ρ_{Co}) and as a mechanism for deep dCo inventory loss driven by higher ρ_{Co}
 960 values. The calculated burial flux of particulate Co within each model variation is also given, but

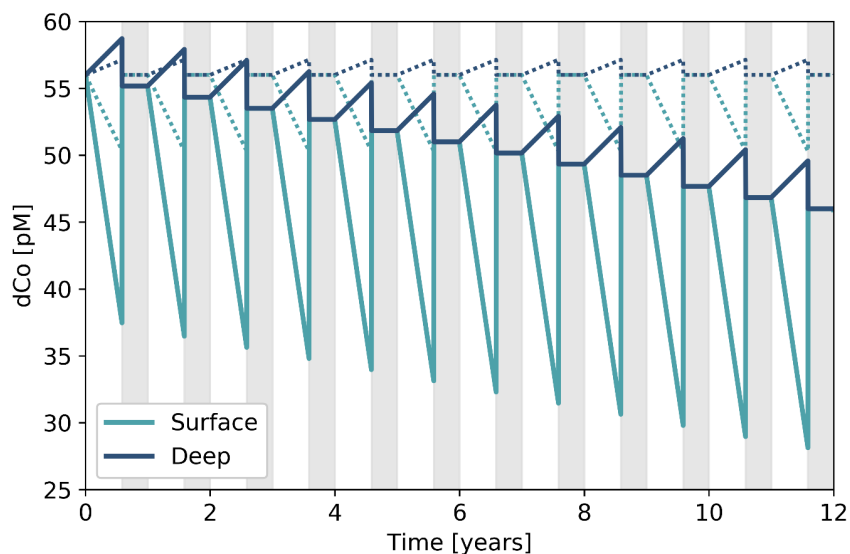


961 note that the burial flux values should be interpreted as a comparison of the Co sink via the
 962 biological pump when ρCo is varied, and not as observed or meaningful Co flux magnitudes.

Model Parameters	Value	Units
Bloom season length	214	days
Surface box height	100	m
Deep box height	500	m
Remineralization Factor (RF)	0.9	
Deep Nephloid Flux	3550	$\text{pmol Co m}^{-2} \text{d}^{-1}$
Overturning Water Flux	0	$\text{m}^3 \text{d}^{-1}$
Steady State Parameters		
Surface ρCo	0.27	$\text{pmol Co L}^{-1} \text{d}^{-1}$
Deep ρCo	0.66	$\text{pmol Co L}^{-1} \text{d}^{-1}$
Burial Flux	3550	$\text{pmol Co m}^{-2} \text{d}^{-1}$
dCo Loss Parameters		
Surface ρCo	0.87	$\text{pmol Co L}^{-1} \text{d}^{-1}$
Deep ρCo	0.1	$\text{pmol Co L}^{-1} \text{d}^{-1}$
Burial Flux	5870	$\text{pmol Co m}^{-2} \text{d}^{-1}$

963

964 This model provides a plausible mechanism by which increases in ρCo such as those
 965 observed along the CICLOPS expedition might increase the burial flux of particulate Co, resulting
 966 in a net loss to the deep dCo inventory. The uptake rate of Co both within and below the photic
 967 zone, as well as the fraction of POM that is remineralized, dictated the flux of particulate Co into
 968 the sediments via burial. The initial dCo concentration was set at 56 pM, which approximates the
 969 mean deep dCo concentrations observed on both CORSACS-1 and CORSACS-2. When the model
 970 was run for 12 years, the time period between the first CORSACS expedition and the CICLOPS
 971 expedition, it generated a sawtooth pattern; the surface and deep boxes diverged over the course
 972 of the summer bloom season as biological uptake removed dCo from the surface box and
 973 remineralization replenished dCo in the deep box (Fig. 12). Winter mixing then unified and reset
 974 the water column, replenishing the surface dCo inventory. The model was run at a steady state
 975 using the average surface ρCo rate observed on CORSACS-1 ($0.27 \text{ pmol L}^{-1} \text{d}^{-1}$; Table 6) (Saito
 976 et al., 2010) and deep ρCo values that were tuned to allow no change in the deep dCo inventory
 977 every winter. When the model was run using representative surface and deep ρCo values observed
 978 on the CICLOPS expedition (0.87 and $0.1 \text{ pmol Co L}^{-1} \text{d}^{-1}$, respectively), the surface depletion of
 979 dCo was more pronounced by the end of the bloom season compared to the steady state model,
 980 and winter mixing resulted in a steady annual decrease of the deep dCo inventory. The mechanism
 981 of dCo loss was driven by increasing ρCo , particularly in the surface ocean, and the propagation
 982 of dCo loss into the deep ocean via vertical mixing. The resulting burial flux when the model
 983 exhibited a deep dCo loss mechanism was higher than when the model was run at a steady state
 984 (Table 6), demonstrating how higher Co uptake rates among plankton paired with a deep winter
 985 mixed layer can result in a diminishing dCo inventory on a decadal timescale.



986

987

988

989

990

991

992

993

994

995

Figure 12. Results of the two-box model illustrating a potential mechanism for the loss of the dCo inventory over time. Gray boxes represent the winter season when the surface and deep boxes mix. The dotted lines represent a system at a steady state, where the dCo inventory stays consistent annually. The solid lines represent a system exhibiting dCo loss, where increased Co uptake rates in both the surface and deep ocean result in an annually decreasing dCo inventory. The initial deep dCo concentration was 56 pM, which approximates the mean deep dCo concentrations observed on CORSACS-1 and CORSACS-2. Over 12 years, the dCo loss model depicts the loss of 0.83 pM year⁻¹ to end at a deep dCo inventory of 46 pM, the mean deep dCo concentration observed on CICLOPS.

996

997

998

999

1000

1001

1002

1003

1004

1005

1006

1007

1008

The purpose of this model was to illustrate a possible mechanism for a dCo inventory loss over the 12-year period between the CORSACS and CICLOPS expeditions using reasonable estimates of Co uptake and other Co cycle fluxes to achieve the observed 10 pM deep inventory loss. This box model successfully shows the directionality of the changes to the deep ocean dCo inventory and deep burial flux when the ρCo values increase, but the magnitude of the estimated Co burial or the nepheloid Co source should not be considered meaningful flux values. The model represented a greatly simplified version of the carbon pump in the Southern Ocean, and it is likely that at least some of the unquantified Co cycle fluxes were not negligible, including horizontal advection, overturning water during the summer season, Co scavenging, and a surface aerosol source. Additionally, it is a simplifying assumption that ρCo values would be consistent throughout a surface or deep depth region, as well as consistent over an entire summer season. Despite its simplicity, the box model presented a concise and reasonable mechanism for this study's observation of a shrinking dCo inventory in the Ross Sea.

1009

5 Conclusion

1010

1011

1012

The Ross Sea, Amundsen Sea and Terra Nova Bay displayed lower dCo and labile dCo inventories during the 2017/2018 austral summer relative to prior observations in the region, which is consistent with observations of higher rates of Co use and uptake by phytoplankton and



1013 heterotrophic bacteria. The near-100% complexation of the dCo inventory reveals that the dCo
1014 loss is primarily due to the uptake of labile dCo, the most bioavailable form of dCo to marine
1015 microbes. The decrease in dCo throughout the water column compared to prior observations is
1016 indicative of a multi-year mechanism, whereby the removal of dCo from the surface mixed layer
1017 via uptake over the summer has been propagated into the deep ocean via winter mixing, resulting
1018 in a decrease in dCo concentration throughout the water column. This change may be due to the
1019 alleviation of Fe limitation through inputs from increased glacial melting and subsequent
1020 development of intermittent vitamin B₁₂ and/or Zn limitation, both of which would be expected to
1021 increase the demand for Co among plankton communities.

1022 In coastal Antarctica and other regions impacted by global climate change, Co is a
1023 noteworthy trace metal nutrient to investigate because its small inventory and flexible
1024 phytoplankton stoichiometry make its biogeochemical cycle particularly vulnerable to
1025 perturbation. In the Arctic Ocean, for example, the dCo and labile dCo inventories have increased
1026 as melting ice and permafrost have increased the flux of Co-enriched riverine waters and sediments
1027 to the upper ocean (Bundy et al., 2020). Like many other trace nutrients, the Co cycle is integrally
1028 connected to that of other elements like Zn, Cd, Fe and carbon, and observations of perturbed Co
1029 inventories and changing nutrient limitation regimes would affect their biogeochemical cycles as
1030 well. In highly productive coastal Antarctic seas, shifts in micronutrient inventories and growth
1031 limitation could have implications for the composition of regional phytoplankton blooms and the
1032 magnitude of the Southern Ocean carbon sink.

1033 Since the late 1980s, it has been hypothesized that the primary productivity and net carbon
1034 sequestration flux of the Southern Ocean is controlled by the supply of Fe to surface waters (Martin
1035 1990; Martin et al., 1990). This theory, called the “iron hypothesis”, posits that the addition of
1036 bioavailable Fe to an Fe-limited surface ocean stimulates productivity and, in turn, increases the
1037 regional and possibly global carbon sequestration flux from the atmosphere into deep ocean
1038 sediments. When applied to potential carbon dioxide removal (CDR) geoengineering projects, the
1039 iron hypothesis provides a theoretical framework for ocean iron fertilization (OIF), where
1040 significant quantities of Fe are introduced to the surface Southern Ocean to enhance the net
1041 sequestration of CO₂ and reduce global atmospheric CO₂ concentrations (Emerson, 2019). Over
1042 the past three decades, several mesoscale Fe fertilization experiments have shown that large
1043 phytoplankton blooms can be stimulated by the addition of Fe to the surface Southern Ocean, and
1044 that the impact on the CO₂ sink is variable, modest and often difficult to assess (Coale et al., 1996;
1045 Boyd et al., 2000; de Baar et al., 2005; Smetacek et al., 2012). This study provides additional
1046 insights into the potential of OIF, suggesting that the alleviation of Fe limitation might shift the
1047 region towards the limitation of another trace nutrient such as vitamin B₁₂, Zn, and potentially Co.
1048 The nutrient limitation regimes of the Southern Ocean are complex, heterogeneous and possibly
1049 shifting on decadal timescales, and these intricacies must be examined when considering future
1050 OIF projects.

1051

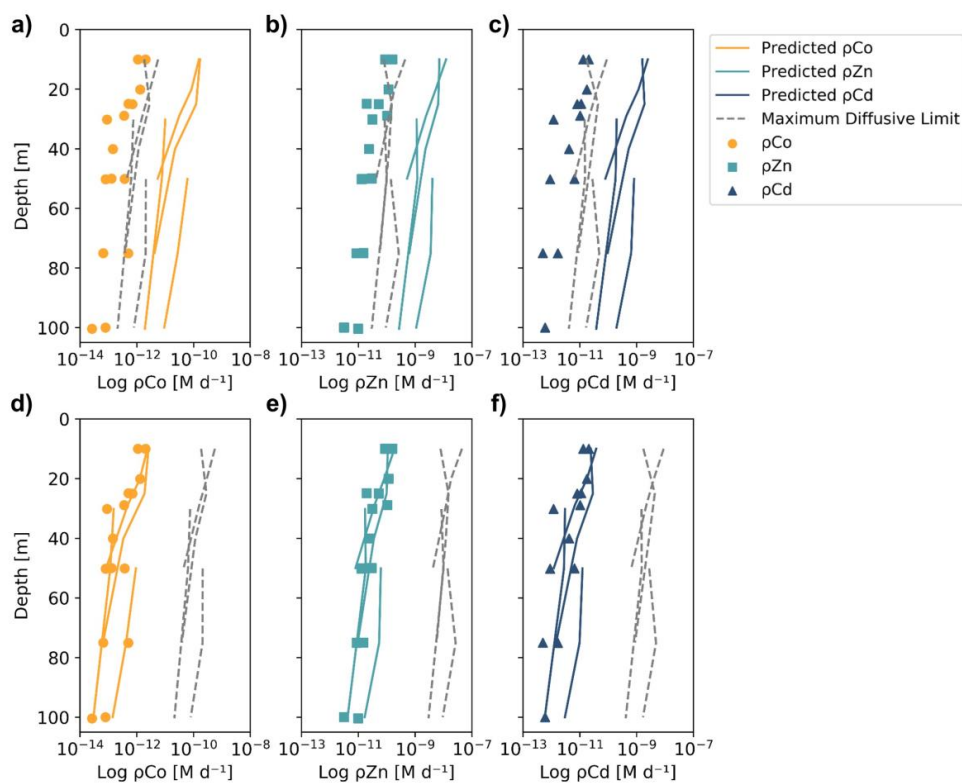
1052

1053

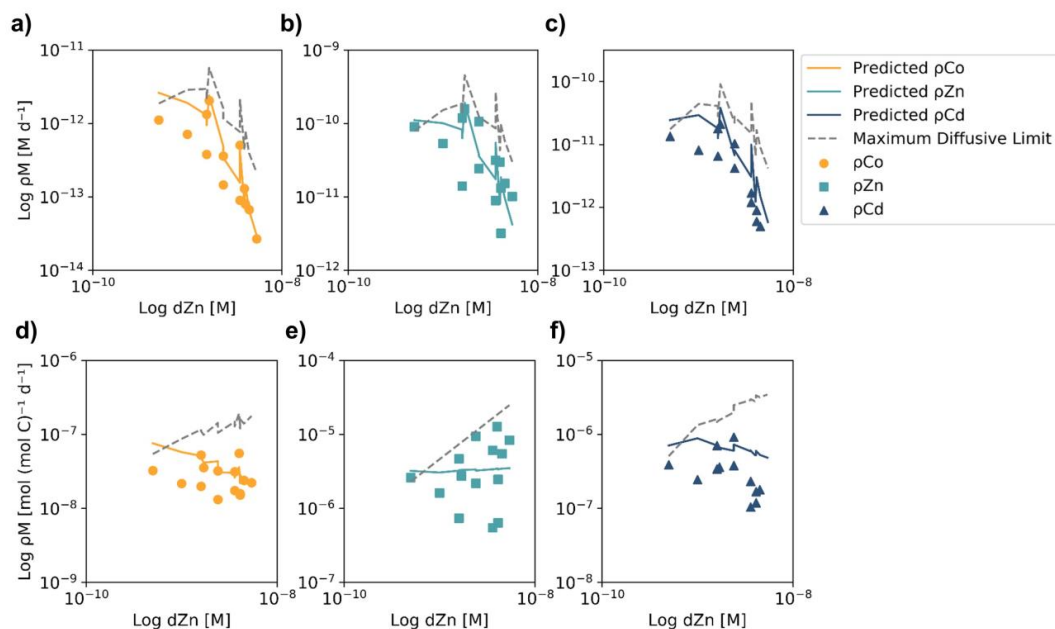
1054



1055 **Appendix A. Estimating trace metal uptake and maximum rate of dissolution profiles from**
 1056 **classic competitive inhibition equations.**



1057 **Figure A1.** Observed (markers) and predicted (solid lines) trace metal uptake rate (ρM) profiles
 1058 and the estimated maximum diffusive limit profiles (dashed line) for Co (**a,d**) Zn (**b,e**) and Cd (**c,f**)
 1059 from Stations 11, 20, 22 and 57, using different equation parameters than those used in Fig. 10. In
 1060 panels a-c, the predicted uptake rates used a literature V_{max} value of $262 \mu\text{mol} (\text{mol C}^{-1}) \text{d}^{-1}$
 1061 determined from Zn^{2+} uptake experiments in *Emiliania huxleyi* cultures (Sunda and Huntsman,
 1062 1992), resulting in predicted uptake rates that were orders of magnitude greater than the observed
 1063 values. In panels d-e, the estimated maximum diffusive limit profiles assumed that 100% of the
 1064 $d\text{Co}$, $d\text{Zn}$ and $d\text{Cd}$ inventories were labile and 0% were bound to strong organic ligands, resulting
 1065 in diffusive limits that were also orders of magnitude greater than the observed values. This
 1066 analysis helps to show how parameter assumptions can greatly influence the predicted uptake rates
 1067 and illustrates the difficulty of assigning kinetic parameters to environmental analyses.
 1068
 1069



1070

1071

1072

1073

1074

1075

1076

1077

1078

1079

1080

1081

1082

Figure A2. Observed (markers) and predicted (solid lines) trace metal uptake rates (ρM) and the estimated maximum diffusive limit profiles (dashed line) plotted against total dZn concentrations, assuming a V_{\max} of $4 \mu\text{mol} (\text{mol C}^{-1}) \text{d}^{-1}$ and that 99% of the trace metal inventory was bound to strong organic ligands. Panels **a-c** show ρM in units of M d^{-1} , which tended to decrease at high dZn concentrations. This is attributable to higher dZn concentrations below the photic zone, where much lower rates of micronutrient uptake occur. Panels **d-f** show ρM when normalized to biomass using Chl-a concentrations and a C : chl-a ratio of 130 w/w (DiTullio and Smith, 1996). The normalized predicted $\rho Z\text{n}$ values are relatively stable over the observed range of dZn concentrations, while the predicted ρCo and ρCd values decrease slightly as dZn increases, suggesting that competitive inhibition of ρCo and ρCd may have occurred at higher dZn concentrations due to the smaller inventories of dCo and dCd compared to dZn.



1083 **Appendix B. Description of a two-box model of the dCo cycle in coastal Antarctic seas, and**
 1084 **a potential mechanism for deep dCo loss with changing microbial uptake stoichiometry.**

1085 The two-box model described below was used to conceptualize the biogeochemical cycling
 1086 of dCo in the surface and deep ocean. The model describes a 1 m² column of water with a total
 1087 depth of 600 m and a depth threshold between the surface and deep box of 100 m. Within each
 1088 box, the net change of dCo over time is equivalent to the sum of the source fluxes minus the sum
 1089 of the sink fluxes:

1090
$$\left(\frac{d[dCo]}{dt}\right)_{Surface} = \frac{\sum(F_i)_{Sources} - \sum(F_i)_{Sinks}}{V_{Surface}}$$

1091
$$\left(\frac{d[dCo]}{dt}\right)_{Deep} = \frac{\sum(F_i)_{Sources} - \sum(F_i)_{Sinks}}{V_{Deep}}$$

1092 where fluxes (F_i) are in units of mols dCo d⁻¹. A summary of the sources and sinks relevant to
 1093 dCo in coastal Antarctic seas is shown below in Table B1. In the Southern Ocean, we would
 1094 expect the fluxes of scavenging (F_{Scav}) and aerosol deposition (F_{Aero}) would be relatively
 1095 negligible, and so these fluxes have been omitted from the model. Additionally, we can assume
 1096 that horizontal advection is at a steady state, and thus the net advection flux is ≈ 0 mols dCo d⁻¹.
 1097 This gives us the net equations for both boxes:

1098
$$\left(\frac{d[dCo]}{dt}\right)_{Surface} = \frac{F_{Over} + F_{Remin} - F_{Up}}{V_{Surface}}$$

1099
$$\left(\frac{d[dCo]}{dt}\right)_{Deep} = \frac{F_{Remin} + F_{Neph} - F_{Up} - F_{Over}}{V_{Deep}}$$

1100 **Table B1:** The source and sink fluxes of dCo in the surface and deep ocean boxes. Fluxes are
 1101 theoretically in units of mols dCo d⁻¹.

Surface Sources	Surface Sinks	Deep Sources	Deep Sinks
Remineralization F_{Remin}	Microbial Uptake F_{Up}	Remineralization F_{Remin}	Microbial Uptake F_{Up}
Overturning F_{Over}	Advection F_{Adv}	Nepheloid Layer F_{Neph}	Overturning F_{Over}
Aerosols F_{Aero}		Advection F_{Adv}	Scavenging F_{Scav}
Advection F_{Adv}			Advection F_{Adv}

1102 Uptake fluxes

1103 The flux of dCo incorporation into microbial biomass via uptake by protein transporters
 1104 can be described using the uptake rates (ρ_{Co}) measured by ⁵⁷Co incubation experiments, where
 1105 units of ρ_{Co} are in mols dCo L⁻¹ d⁻¹:
 1106

1107
$$F_{Up, Surface} = (\rho_{Co} o_{Surface} * V_{Surface})$$

1108
$$F_{Up, Deep} = (\rho_{Co} o_{Deep} * V_{Deep})$$

1109

1110

1111



1112 Remineralization fluxes

1113 In this model, the remineralization flux of particulate Co in organic matter to dCo is
 1114 quantified by a Remineralization Factor (RF), which can be applied to the amount of particulate
 1115 matter present in each box. Typical RF values tend to be between 0.90 and 0.99 (Glover et al.,
 1116 2011), meaning that between 90% and 99% of all microbial biomass produced tends to be
 1117 remineralized before sinking out of its respective box. It is not clear that the RFs for the surface
 1118 and deep box should be represented by the same value, and so we have defined both surface
 1119 ($RF_{Surface}$) and deep (RF_{deep}) variables here. In the surface ocean, excess Co in un-remineralized
 1120 biomass will sink into the deep box (F_{Sink}), where it is further able to be remineralized in the deep
 1121 ocean. In the deep ocean, excess Co in un-remineralized biomass is assumed to flux into the
 1122 sediments via burial (F_{Bur}), representing a key sink of dCo biomass out of the two-box system. The
 1123 surface box remineralization flux is represented with a relatively simple equation:

$$1124 \quad F_{Remin, Surface} = RF_{Surface} * F_{Up, Surface}$$

$$1125 \quad F_{Remin, Surface} = RF_{Surface}(\rho C_{O_{Surface}} * V_{Surface})$$

1126 The deep ocean remineralization flux can then be calculated as the sum of the
 1127 remineralization flux from excess biomass that sinks as particulate Co and biomass generated in
 1128 the deep ocean:

$$1129 \quad F_{Remin, Deep} = RF_{Deep}(F_{Up, Surface} - F_{Remin, Surface}) + RF_{Deep}(F_{Up, Deep})$$

$$1130 \quad F_{Remin, Deep} = RF_{Deep}(\rho C_{O_{Surface}} * V_{Surface} - RF_{Surface}(\rho C_{O_{Surface}} * V_{Surface}))$$

$$1131 \quad + RF_{Deep}(\rho C_{O_{Deep}} * V_{Deep})$$

1132 Overturning fluxes

1133 An overturning dCo flux represents the flux of a volume of water from the deep ocean box
 1134 into the shallow ocean box, and a corresponding flux of the same volume from the shallow ocean
 1135 box into the deep ocean box for mass conservation. In a dynamic coastal upwelling system like
 1136 the Ross and Amundsen Seas, the reality of this overturning flux is almost certainly much more
 1137 complicated, as coastal upwelling processes overlap with meltwater processes and deep water mass
 1138 formation processes. For the purposes of this two-box model, the flux of dCo via overturning can
 1139 be estimated as a function of the overturning water flux (F_{Water}) and the dCo concentrations of each
 1140 box:

$$1141 \quad F_{Over, Surface} = (F_{Water}[dCo]_{Deep} - F_{Water}[dCo]_{Surface})$$

$$1142 \quad F_{Over, Deep} = (F_{Water}[dCo]_{Surface} - F_{Water}[dCo]_{Deep})$$

1143 In the model presented in Sect. 4.6, the F_{Water} and both F_{Over} fluxes are assumed to be
 1144 negligible for the sake of modeling simplicity, but the introduction of a nonzero overturning flux
 1145 would help to make the seasonal change in the dCo inventory in both the surface and deep oceans
 1146 nonlinear, as it is currently the only flux in this model that is calculated using the time step's dCo
 1147 concentrations.

1148 Flux from the nepheloid layer

1149 At several CICLOPS stations, a distinct nepheloid layer was detected as dCo concentration
 1150 increased sharply at depths immediately above (~10 m) the ocean floor. The nepheloid layer tends



1151 to contain high levels of particles moving horizontally along the seafloor, and is likely a significant
1152 source of dCo to the surrounding water column. The source of dCo from the nepheloid layer is
1153 somewhat unclear; it could be via dissolution of particles suspended within the nepheloid layer or
1154 from a porewater flux of dCo out of the sediments. In this model, the flux of deep dCo inputs into
1155 the deep ocean, assumed to be from the nepheloid layer, was derived using the Microsoft Excel
1156 solver tool, given the parameter that 10 pM of deep dCo was lost over 12 years. The deep source
1157 of dCo was calculated to be 3550 pmol dCo m⁻² d⁻¹. This value should be considered an adjustable
1158 parameter used to tune the model to our conceptual understanding of dCo inventory loss, and not
1159 a meaningful calculation of observed Co flux from the deep nepheloid layer, which has yet to be
1160 constrained.

1161 **The cobalt burial sink**

1162 The loss of cobalt from the deep ocean box into the sediments via burial can be quantified
1163 with the equation:

$$1164 \left(\frac{d[Co]}{dt} \right)_{Bur} = F_{Sink} + F_{Up,Deep} - F_{Remin,Deep}$$

1165 where F_{Sink} is described by:

$$1166 F_{Sink} = (\rho C_{O_{Surface}} * V_{Surface}) - R F_{Surface} (\rho C_{O_{Surface}} * V_{Surface})$$

1167 This estimate of the loss of dCo due to burial assumes that all biogenic particulate Co that is not
1168 remineralized in the surface ocean sinks into the deep ocean, and all biogenic particulate Co that
1169 is not remineralized in the deep ocean is sequestered in sediments and “lost” to the model.

1170 **Modeling seasonality: the winter mixed layer**

1171 In the Ross and Amundsen Seas, sea ice covers the surface ocean for a larger portion of the
1172 year (~ 5 months). During this time, the water column mixes – a process that was modeled by
1173 combining the two-box model into one homogenized box after the 7-month bloom season to
1174 simulate the winter season. This process can be modeled by a volume-weighted average with the
1175 volume of each box.

$$1176 [dCo]_{Winter} = \frac{(V_{Surface} * [dCo]_{Surface}) + (V_{Deep} * [dCo]_{Deep})}{(V_{Surface} + V_{Deep})}$$

1177 **Data availability**

1178 The CICLOPS dCo dataset has been submitted to the Biological and Chemical Oceanography Data
1179 Management Office (BCO-DMO) website (<https://www.bco-dmo.org/project/774945>) and is
1180 pending approval for publication. The dissolved metals (dZn, dCd) dataset (<https://www.bco-dmo.org/dataset/877466>),
1181 Zn and Cd uptake rate dataset (<https://www.bco-dmo.org/dataset/877681>), and macronutrient dataset (<https://www.bco-dmo.org/dataset/874841>)
1182 are publicly available on the BCO-DMO website.
1183

1184 **Author contribution**

1185 RC collected and analyzed dCo samples and wrote the manuscript. RK collected and analyzed
1186 dZn and dCd samples and measured Zn and Cd uptake rates. DR measured Co uptake rates. GD



1187 collected and analyzed phytoplankton pigment samples. All authors assisted in the collection and
1188 processing of dissolved seawater samples and incubation experiment samples, and all authors
1189 helped write the manuscript.

1190 **Competing interests**

1191 The authors declare that they have no conflict of interest.

1192 **Acknowledgments**

1193 The authors thank the captain, crew and science party of the RVIB *Nathaniel B. Palmer* for their
1194 support during the CICLOPS expedition. We also thank Joe Jennings (OSU) for dissolved
1195 macronutrient analysis, Véronique Oldham for sampling assistance, and Matthew Charette,
1196 Stephanie Dutkiewicz, and Alessandro Tagliabue for writing insights. This work was funded by
1197 grants from the National Science Foundation's Office of Polar Programs (OPP-1643684, OPP-
1198 1644073 and OPP-1643845).

1199 **References**

- 1200 Arrigo, K. R., Robinson, D. H., Worthen, D. L., Dunbar, R. B., DiTullio, G. R., Vanwoert, M.
1201 and Lizotte, M. P.: Phytoplankton community structure and the drawdown of nutrients and CO₂
1202 in the Southern Ocean, *Science.*, 283, 365–367, 1999.
- 1203 Arrigo, K. R., van Dijken, G. L. and Bushinsky, S.: Primary production in the Southern Ocean,
1204 1997-2006, *J. Geophys. Res.*, 113, C08004, doi:10.1029/2007JC004551, 2008.
- 1205 Arrigo, K. R., Lowry, K. E. and van Dijken, G. L.: Annual changes in sea ice and phytoplankton
1206 in polynyas of the Amundsen Sea, Antarctica, *Deep. Res. Part II Top. Stud. Oceanogr.*, 71–76,
1207 5–15, doi:10.1016/j.dsr2.2012.03.006, 2012.
- 1208 de Baar, H. J. W., Boyd, P. W., Coale, K. H., Landry, M. R., Tsuda, A., Assmy, P., Bakker, D.
1209 C. E., Bozec, Y., Barber, R. T., Brzezinski, M. A., Buesseler, K. O., Boyé, M., Croot, P. L.,
1210 Gervais, F., Gorbunov, M. Y., Harrison, P. J., Hiscock, W. T., Laan, P., Lancelot, C., Law, C. S.,
1211 Lavoie, M., Marchetti, A., Millero, F. J., Nishioka, J., Nojiri, Y., van Oijen, T., Riebesell, U.,
1212 Rijkenberg, M. J. A., Saito, H., Takeda, S., Timmermans, K. R., Veldhuis, M. J. W., Waite, A.
1213 M. and Wong, C. S.: Synthesis of iron fertilization experiments: From the iron age in the age of
1214 enlightenment, *J. Geophys. Res. C Ocean.*, 110(9), 1–24, doi:10.1029/2004JC002601, 2005.
- 1215 Bernhardt, H. and Wilhelms, A.: The continuous determination of low level iron, soluble
1216 phosphate and total phosphate with the AutoAnalyzer(TM), in *Technicon Symposium*, vol. 1, p.
1217 386., 1967.
- 1218 Bertrand, E. M., Saito, M. A., Rose, J. M., Riesselman, C. R., Lohan, M. C., Noble, A. E., Lee,
1219 P. A. and DiTullio, G. R.: Vitamin B12 and iron colimitation of phytoplankton growth in the
1220 Ross Sea, *Limnol. Oceanogr.*, 52(3), 1079–1093, doi:10.4319/lo.2007.52.3.1079, 2007.
- 1221 Bertrand, E. M., Saito, M. A., Lee, P. A., Dunbar, R. B., Sedwick, P. N. and DiTullio, G. R.: Iron
1222 limitation of a springtime bacterial and phytoplankton community in the Ross Sea: implications
1223 for vitamin B12 nutrition, *Front. Microbiol.*, 2, 160, doi:10.3389/fmicb.2011.00160, 2011.
- 1224 Bertrand, E. M., Moran, D. M., McIlvin, M. R., Hoffman, J. M., Allen, A. E. and Saito, M. A.:
1225 Methionine synthase interreplacement in diatom cultures and communities: Implications for the



- 1226 persistence of B12 use by eukaryotic phytoplankton, *Limnol. Oceanogr.*, 58(4), 1431–1450,
1227 doi:10.4319/lo.2013.58.4.1431, 2013.
- 1228 Bown, J., Boye, M. and Nelson, D. M.: New insights on the role of organic speciation in the
1229 biogeochemical cycle of dissolved cobalt in the southeastern Atlantic and the Southern Ocean,
1230 *Biogeosciences*, 9, 2719–2736, doi:10.5194/bg-9-2719-2012, 2012.
- 1231 Boyd, P. W., Watson, A. J., Law, C. S., Abraham, E. R., Trull, T., Murdoch, R., Bakker, D. C.
1232 E., Bowie, A. R., Buesseler, K. O., Chang, H., Charette, M., Croot, P., Downing, K., Frew, R.,
1233 Gall, M., Hadfield, M., Hall, J., Harvey, M., Jameson, G., LaRoche, J., Liddicoat, M., Ling, R.,
1234 Maldonado, M. T., McKay, R. M., Nodder, S., Pickmere, S., Pridmore, R., Rintoul, S., Safi, K.,
1235 Sutton, P., Strzepek, R., Tanneberger, K., Turner, S., Waite, A. and Zeldis, J.: A mesoscale
1236 phytoplankton bloom in the polar Southern Ocean stimulated by iron fertilization, *Nature*,
1237 407(6805), 695–702, doi:10.1038/35037500, 2000.
- 1238 Brisbin, M. M., Mitarai, S., Saito, M. A. and Alexander, H.: Microbiomes of bloom-forming
1239 *Phaeocystis* algae are stable and consistently recruited, with both symbiotic and opportunistic
1240 modes, *ISME J*, doi:10.1038/s41396-022-01263-2, 2022.
- 1241 Budillon, G., Salusti, E. and Tucci, S.: The evolution of density currents and nepheloid bottom
1242 layers in the Ross Sea (Antarctica), *J. Mar. Res.*, 64(4), 517–540,
1243 doi:10.1357/002224006778715739, 2006.
- 1244 Bundy, R. M., Tagliabue, A., Hawco, N. J., Morton, P. L., Twining, B. S., Hatta, M., Noble, A.,
1245 Cape, M. R., John, S. G., Cullen, J. T. and Saito, M. A.: Elevated sources of cobalt in the Arctic
1246 Ocean, *Biogeosciences*, 17, 4745–4767, doi:https://doi.org/10.5194/bg-2020-84, 2020.
- 1247 Caron, D. A., Dennett, M. R., Lonsdale, D. J., Moran, D. M. and Shalapyonok, L.:
1248 Microzooplankton herbivory in the Ross Sea, Antarctica, *Deep Sea Res. II*, 47, 3249–3272,
1249 2000.
- 1250 Chandler, J. W., Lin, Y., Gainer, P. J., Post, A. F., Johnson, Z. I. and Zinser, E. R.: Variable but
1251 persistent coexistence of *Prochlorococcus* ecotypes along temperature gradients in the ocean’s
1252 surface mixed layer, *Environ. Microbiol. Rep.*, 8(2), 272–284, doi:10.1111/1758-2229.12378,
1253 2016.
- 1254 Chappell, P. D., Vedmati, J., Selph, K. E., Cyr, H. A., Jenkins, B. D., Landry, M. R. and Moffett,
1255 J. W.: Preferential depletion of zinc within Costa Rica upwelling dome creates conditions for
1256 zinc co-limitation of primary production, *J. Plankton Res.*, 38(2), 244–255,
1257 doi:10.1093/plankt/fbw018, 2016.
- 1258 Chmiel, R., Lanning, N., Laubach, A., Lee, J.-M., Fitzsimmons, J., Hatta, M., Jenkins, W. J.,
1259 Lam, P. J., Mcilvin, M., Tagliabue, A. and Saito, M. A.: Major processes of the dissolved cobalt
1260 cycle in the North and equatorial Pacific Ocean, *Biogeosciences*, 19, 2365–2395 [online]
1261 Available from: <https://doi.org/10.5194/bg-19-2365-2022>, 2022.
- 1262 Church, M. J., Hutchins, D. A. and Ducklow, H. W.: Limitation of bacterial growth by dissolved
1263 organic matter and iron in the Southern Ocean, *Appl. Environ. Microbiol.*, 66(2), 455–466,
1264 doi:10.1128/AEM.66.2.455-466.2000, 2000.
- 1265 Coale, K. H., Johnson, K. S., Fitzwater, S. E., Gordon, R. M., Tanner, S., Chavez, F. P., Ferioli,
1266 L., Sakamoto, C., Rogers, P., Millero, F., Steinberg, Pa., Nightingale, P., Cooper, D., Cochlan,
1267 W. P., Landry, M. R., Constantinou, J., Rollwagen, G., Trasvina, A. and Kudela, R.: A massive



- 1268 phytoplankton bloom induced by an ecosystem-scale iron fertilization experiment in the
1269 equatorial Pacific Ocean, *Nature*, 383(334), 495–501, 1996.
- 1270 Cohen, N. R., McIlvin, M. R., Moran, D. M., Held, N. A., Saunders, J. K., Hawco, N. J.,
1271 Brosnahan, M., DiTullio, G. R., Lamborg, C., McCrow, J. P., Dupont, C. L., Allen, A. E. and
1272 Saito, M. A.: Dinoflagellates alter their carbon and nutrient metabolic strategies across
1273 environmental gradients in the central Pacific Ocean, *Nat. Microbiol.*, 6, 173–186,
1274 doi:10.1038/s41564-020-00814-7, 2021.
- 1275 Croft, M. T., Lawrence, A. D., Raux-deery, E., Warren, M. J. and Smith, A. G.: Algae acquire
1276 vitamin B12 through a symbiotic relationship with bacteria, *Nature*, 438, 90–93,
1277 doi:10.1038/nature04056, 2005.
- 1278 DiTullio, G. and Geesey, M. E.: Photosynthetic Pigments in Marine Algae and Bacteria, in
1279 *Encyclopedia of Environmental Microbiology*, edited by G. Bitton, pp. 2453–2470, John Wiley
1280 & Sons, Inc., New York, NY., 2003.
- 1281 DiTullio, G. R., Grebmeier, J. M., Arrigo, K. R. and Lizotte, M. P.: Rapid and early export of
1282 *Phaeocystis antarctica* blooms in the Ross Sea, Antarctica, *Nature*, 404, 595–598, 2000.
- 1283 DiTullio, G. R. and Smith, W. O. J.: Spatial patterns in phytoplankton biomass and pigment
1284 distributions in the Ross Sea, *J. Geophys. Res.*, 101, 18467–18477, 1996.
- 1285 DiTullio, G. R., Geesey, M. E., Jones, D. R., Daly, K. L., Campbell, L. and Smith, W. O. J.:
1286 Phytoplankton assemblage structure and primary productivity along 170° W in the South Pacific
1287 Ocean, *Mar. Ecol. Prog. Ser.*, 255, 55–80, 2003.
- 1288 DiTullio, G. R., Garcia, N., Riseman, S. F. and Sedwick, P. N.: Effects of iron concentration on
1289 pigment composition in *Phaeocystis antarctica* grown at low irradiance, *Biogeochemistry*, 83,
1290 71–81, doi:10.1007/s10533-007-9080-8, 2007.
- 1291 Ducklow, H., Carlson, C., Church, M., Kirchman, D., Smith, D. and Steward, G.: The seasonal
1292 development of the bacterioplankton bloom in the Ross Sea, Antarctica, 1994–1997, *Deep. Res.*
1293 *Part II*, 48, 4199–4221, 2001.
- 1294 Ellwood, M. J., Van Den Berg, C. M. G., Boye, M., Veldhuis, M., de Jong, J. T. M., de Baar, H.
1295 J. W., Croot, P. L. and Kattner, G.: Organic complexation of cobalt across the Antarctic Polar
1296 Front in the Southern Ocean, *Mar. Freshw. Res.*, 56, 1069–1075, doi:10.1071/MF05097, 2005.
- 1297 Emerson, D.: Biogenic iron dust: A novel approach to ocean iron fertilization as a means of large
1298 scale removal of carbon dioxide from the atmosphere, *Front. Mar. Sci.*, 6, 22,
1299 doi:10.3389/fmars.2019.00022, 2019.
- 1300 Fitzwater, S. E., Johnson, K. S., Gordon, R. M., Coale, K. H. and Smith, W. O.: Trace metal
1301 concentrations in the Ross Sea and their relationship with nutrients and phytoplankton growth,
1302 *Deep. Res. Part II*, 47, 3159–3179, 2000.
- 1303 Gardner, W. D., Richardson, M. J. and Mishonov, A. V.: Global assessment of benthic nepheloid
1304 layers and linkage with upper ocean dynamics, *Earth Planet. Sci. Lett.*, 482, 126–134,
1305 doi:10.1016/j.epsl.2017.11.008, 2018.
- 1306 Glover, D., Jenkins, W. and Doney, S.: *Modeling Methods for Marine Science*, Cambridge
1307 University Press, New York., 2011.



- 1308 Hawco, N. J., Ohnemus, D. C., Resing, J. A., Twining, B. S. and Saito, M. A.: A dissolved cobalt
1309 plume in the oxygen minimum zone of the eastern tropical South Pacific, *Biogeosciences*,
1310 13(20), 5697–5717, doi:10.5194/bg-13-5697-2016, 2016.
- 1311 Hawco, N. J., Lam, P. J., Lee, J., Ohnemus, D. C., Noble, A. E., Wyatt, N. J., Lohan, M. C. and
1312 Saito, M. A.: Cobalt scavenging in the mesopelagic ocean and its influence on global mass
1313 balance: Synthesizing water column and sedimentary fluxes, *Mar. Chem.*, (August),
1314 doi:10.1016/j.marchem.2017.09.001, 2017.
- 1315 Helliwell, K. E.: The roles of B vitamins in phytoplankton nutrition: new perspectives and
1316 prospects, *New Phytol.*, 216, 62–68, doi:10.1111/nph.14669, 2017.
- 1317 Irving, H. and Williams, R. J. P.: Order of stability of metal complexes, *Nature*, 162, 746–747,
1318 1948.
- 1319 Jakuba, R. W., Moffett, J. W. and Dyrhman, S. T.: Evidence for the linked biogeochemical
1320 cycling of zinc, cobalt, and phosphorus in the western North Atlantic Ocean, *Global Biogeochem.*
1321 *Cycles*, 22(4), GB4012, doi:10.1029/2007GB003119, 2008.
- 1322 Jakuba, R. W., Saito, M. A., Moffett, J. W. and Xu, Y.: Dissolved zinc in the subarctic North
1323 Pacific and Bering Sea: Its distribution, speciation, and importance to primary producers, *Global*
1324 *Biogeochem. Cycles*, 26, GB2015, doi:10.1029/2010GB004004, 2012.
- 1325 John, S. G., Geis, R. W., Saito, M. A. and Boyle, E. A.: Zinc isotope fractionation during high-
1326 affinity and low-affinity zinc transport by the marine diatom *Thalassiosira oceanica*, *Limnol.*
1327 *Oceanogr.*, 52(6), 2710–2714, doi:10.4319/lo.2007.52.6.2710, 2007.
- 1328 Kellogg, R. M.: Assessing the potential for Zn limitation of marine primary production:
1329 proteomic characterization of the low Zn stress response in marine diatoms, Massachusetts
1330 Institute of Technology; the Woods Hole Oceanographic Institution., 2022.
- 1331 Kellogg, R. M., McIlvin, M. R., Vedamati, J., Twining, B. S., Moffett, J. W., Marchetti, A.,
1332 Moran, D. M. and Saito, M. A.: Efficient zinc/cobalt interreplacement in northeast Pacific
1333 diatoms and relationship to high surface dissolved Co : Zn ratios, *Limnol. Oceanogr.*, 65(11),
1334 2557–2582, doi:10.1002/lno.11471, 2020.
- 1335 Kellogg, R. M., Moosburner, M. A., Cohen, N. R., Hawco, N. J., McIlvin, M. R., Moran, D. M.,
1336 DiTullio, G. R., Subhas, A. V., Allen, A. E. and Saito, M. A.: Adaptive responses of marine
1337 diatoms to zinc scarcity and ecological implications, *Nat. Commun.*, 13, doi:10.1038/s41467-
1338 022-29603-y, 2022.
- 1339 Kellogg, R. M., Schanke, N. L., Lees, L. E., Chmiel, R. J., Rao, D., Brisbin, M. M., Moran, D.
1340 M., McIlvin, M. R., Bolinesi, F., Casotti, R., Balestra, C., Horner, T. J., Subhas, A. V., Dunbar,
1341 R. B., Allen, A. E., DiTullio, G. R. and Saito, M. A.: Zinc co-limitation of natural marine
1342 phytoplankton assemblages in coastal Antarctica [Submitted].
- 1343 Lane, T. W., Saito, M. A., George, G. N., Pickering, I. J., Prince, R. C. and Morel, F. M. M.: A
1344 cadmium enzyme from a marine diatom, *Nature*, 435, 42–42,
1345 doi:https://doi.org/10.1038/435042a, 2005.
- 1346 Lee, J. G. and Morel, F. M. M.: Replacement of zinc by cadmium in marine phytoplankton, *Mar.*
1347 *Ecol. Prog. Ser.*, 127, 305–309, doi:10.3354/meps127305, 1995.



- 1348 Marsay, C. M., Sedwick, P. N., Dinniman, M. S., Barrett, P. M., Mack, S. L. and McGillicuddy,
1349 D. J.: Estimating the benthic efflux of dissolved iron on the Ross Sea continental shelf, *Geophys.*
1350 *Res. Lett.*, 41(21), 7576–7583, doi:10.1002/2014GL061684, 2014.
- 1351 Martin, J. H.: Glacial-interglacial CO₂ change: the iron hypothesis, *Paleoceanography*, 5(1), 1–
1352 13, doi:<https://doi.org/10.1029/PA005i001p00001>, 1990.
- 1353 Martin, J. H., Fitzwater, S. E. and Gordon, R. M.: Iron deficiency limits phytoplankton growth in
1354 Antarctic waters, *Global Biogeochem. Cycles*, 4(1), 5–12, 1990.
- 1355 Mazzotta, M. G., McIlvin, M. R., Moran, D. M., Wang, D. T., Bidle, K. D., Lamborg, C. H. and
1356 Saito, M. A.: Characterization of the metalloproteome of *Pseudoalteromonas* (BB2-AT2):
1357 biogeochemical underpinnings for zinc, manganese, cobalt, and nickel cycling in a ubiquitous
1358 marine heterotroph, *Metallomics*, 13, mfab060, doi:<https://doi.org/10.1093/mtomcs/mfab060>,
1359 2021.
- 1360 Monien, D., Monien, P., Brünjes, R., Widmer, T., Kappenberg, A., Silva Busso, A. A.,
1361 Schnetger, B. and Brumsack, H.-J.: Meltwater as a source of potentially bioavailable iron to
1362 Antarctica waters, *Antarct. Sci.*, 29(03), 277–291, doi:10.1017/S095410201600064X, 2017.
- 1363 Morel, F. M. M., Reinfelder, J. R., Roberts, S. B., Chamberlain, C. P., Lee, J. G. and Yee, D.:
1364 Zinc and carbon co-limitation of marine phytoplankton, *Nature*, 369(6483), 740–742,
1365 doi:10.1038/369740a0, 1994.
- 1366 Morel, F. M. M., Lam, P. J. and Saito, M. A.: Trace Metal Substitution in Marine Phytoplankton,
1367 *Annu. Rev. Earth Planet. Sci.*, 48, 491–517, doi:10.1146/annurev-earth-053018-060108, 2020.
- 1368 Noble, A. E., Saito, M. A., Maiti, K. and Benitez-Nelson, C. R.: Cobalt, manganese, and iron
1369 near the Hawaiian Islands: A potential concentrating mechanism for cobalt within a cyclonic
1370 eddy and implications for the hybrid-type trace metals, *Deep. Res. Part II Top. Stud. Oceanogr.*,
1371 55(10–13), 1473–1490, doi:10.1016/j.dsr2.2008.02.010, 2008.
- 1372 Noble, A. E., Moran, D. M., Allen, A. E. and Saito, M. A.: Dissolved and particulate trace metal
1373 micronutrients under the McMurdo Sound seasonal sea ice: basal sea ice communities as a
1374 capacitor for iron, *Front. Chem.*, 1, 25, doi:10.3389/fchem.2013.00025, 2013.
- 1375 Noble, A. E., Ohnemus, D. C., Hawco, N. J., Lam, P. J. and Saito, M. A.: Coastal sources, sinks
1376 and strong organic complexation of dissolved cobalt within the US North Atlantic GEOTRACES
1377 transect GA03, *Biogeosciences*, 14(11), 2715–2739, doi:10.5194/bg-14-2715-2017, 2017.
- 1378 Oldham, V. E., Chmiel, R., Hansel, C. M., DiTullio, G. R., Rao, D. and Saito, M.: Inhibited
1379 manganese oxide formation hinders cobalt scavenging in the Ross Sea, *Global Biogeochem.*
1380 *Cycles*, 35, e2020GB006706, doi:10.1029/2020GB006706, 2021.
- 1381 Osman, D., Cooke, A., Young, T. R., Deery, E., Robinson, N. J. and Warren, M. J.: The
1382 requirement for cobalt in vitamin B12: A paradigm for protein metalation, *Biochim. Biophys.*
1383 *Acta - Mol. Cell Res.*, 1868, 118896, doi:10.1016/j.bbamcr.2020.118896, 2021.
- 1384 Pelouquin, J. A. and Smith, W. O. J.: Phytoplankton blooms in the Ross Sea, Antarctica:
1385 Interannual variability in magnitude, temporal patterns, and composition, *J. Geophys. Res.*, 112,
1386 C08013, doi:10.1029/2006JC003816, 2007.



- 1387 Planquette, H., Sherrell, R. M., Stammerjohn, S. and Field, M. P.: Particulate iron delivery to the
1388 water column of the Amundsen Sea, Antarctica, *Mar. Chem.*, 153, 15–30,
1389 doi:10.1016/j.marchem.2013.04.006, 2013.
- 1390 Price, N. M., Harrison, G. I., Hering, J. G., Hudson, R. J., Pascale, M., Nirel, V., Palenik, B. and
1391 Morel, F. M. M.: Preparation and Chemistry of the Artificial Algal Culture Medium Aquil, *Biol.*
1392 *Oceanogr.*, 6, 443–461, 2013.
- 1393 Rao, D.: Characterizing cobalamin cycling by Antarctic marine microbes across multiple scales,
1394 Massachusetts Institute of Technology; the Woods Hole Oceanographic Institution., 2020.
- 1395 Rao, D., Fussy, Z., Moran, D. M., McIlvin, M. R., Allen, A. E., Follows, M. J. and Saito, M. A.:
1396 Flexible B12 ecophysiology of *Phaeocystis antarctica* to a fusion B12-independent methionine
1397 synthase with widespread homologues [In review]., *PNAS* [online] Available from:
1398 <http://arxiv.org/abs/1712.09707>.
- 1399 Roberts, S. B., Lane, T. W. and Morel, F. M. M.: Carbonic Anhydrase in the Marine Diatom
1400 *Thalassiosira weissflogii* (Bacillariophyceae), *J. Phycol.*, 33(5), 845–850, doi:10.1111/j.0022-
1401 3646.1997.00845.x, 1997.
- 1402 Rodionov, D. A., Vitreschak, A. G., Mironov, A. A. and Gelfand, M. S.: Comparative genomics
1403 of the vitamin B12 metabolism and regulation in prokaryotes, *J. Biol. Chem.*, 278(42), 41148–
1404 41159, doi:10.1074/jbc.M305837200, 2003.
- 1405 Rose, J. M., Feng, Y., DiTullio, G. R., Dunbar, R. B., Hare, C. E., Lee, P. A., Lohan, M., Long,
1406 M., Smith, W. O., Sohst, B., Tozzi, S., Zhang, Y. and Hutchins, D. A.: Synergistic effects of iron
1407 and temperature on Antarctic phytoplankton and microzooplankton assemblages,
1408 *Biogeosciences*, 6, 3131–3147, doi:10.5194/bg-6-3131-2009, 2009.
- 1409 Saito, M. A. and Goepfert, T. J.: Zinc-cobalt colimitation of *Phaeocystis antarctica*, *Limnol.*
1410 *Oceanogr.*, 53(1), 266–275, 2008.
- 1411 Saito, M. A. and Moffett, J. W.: Complexation of cobalt by natural organic ligands in the
1412 Sargasso Sea as determined by a new high-sensitivity electrochemical cobalt speciation method
1413 suitable for open ocean work, *Mar. Chem.*, 75(1–2), 49–68, doi:10.1016/S0304-4203(01)00025-
1414 1, 2001.
- 1415 Saito, M. A., Rocap, G. and Moffett, J. W.: Production of cobalt binding ligands in a
1416 *Synechococcus* feature at the Costa Rica upwelling dome, *Limnol. Oceanogr.*, 50(1), 279–290,
1417 2005.
- 1418 Saito, M. A., Goepfert, T. J., Noble, A. E., Bertrand, E. M., Sedwick, P. N. and DiTullio, G. R.:
1419 A seasonal study of dissolved cobalt in the Ross Sea, Antarctica: micronutrient behavior,
1420 absence of scavenging, and relationships with Zn, Cd, and P, *Biogeosciences*, 7, 4059–4082,
1421 doi:10.5194/bg-7-4059-2010, 2010.
- 1422 Saito, M. A., Noble, A. E., Hawco, N., Twining, B. S., Ohnemus, D. C., John, S. G., Lam, P.,
1423 Conway, T. M., Johnson, R., Moran, D. and McIlvin, M.: The acceleration of dissolved cobalt's
1424 ecological stoichiometry due to biological uptake, remineralization, and scavenging in the
1425 Atlantic Ocean, *Biogeosciences*, 14(20), 4637–4662, doi:10.5194/bg-14-4637-2017, 2017.



- 1426 Sañudo-Wilhelmy, S. A., Gobler, C. J., Okbamichael, M. and Taylor, G. T.: Regulation of
1427 phytoplankton dynamics by vitamin B12, *Geophys. Res. Lett.*, 33(4), 10–13,
1428 doi:10.1029/2005GL025046, 2006.
- 1429 Sedwick, P. N. and DiTullio, G. R.: Regulation of algal blooms in Antarctic shelf waters by the
1430 release of iron from melting sea ice, *Geophys. Reseach Lett.*, 24(20), 2515–2518, 1997.
- 1431 Sedwick, P. N., DiTullio, G. R. and Mackey, D. J.: Iron and manganese in the Ross Sea,
1432 Antarctica: Seasonal iron limitation in Antarctic shelf waters, *J. Geophys. Res.*, 105(C5), 11321–
1433 11336, 2000.
- 1434 Sedwick, P. N., Marsay, C. M., Sohst, B. M., Aguilar-Islas, A. M., Lohan, M. C., Long, M. C.,
1435 Arrigo, K. R., Dunbar, R. B., Saito, M. A., Smith, W. O. and DiTullio, G. R.: Early season
1436 depletion of dissolved iron in the Ross Sea polynya: Implications for iron dynamics on the
1437 Antarctic continental shelf, *J. Geophys. Res.*, 116, C12019, doi:10.1029/2010JC006553, 2011.
- 1438 Smetacek, V., Klaas, C., Strass, V. H., Assmy, P., Montresor, M., Cisewski, B., Savoye, N.,
1439 Webb, A., D’Ovidio, F., Arrieta, J. M., Bathmann, U., Bellerby, R., Berg, G. M., Croot, P.,
1440 Gonzalez, S., Henjes, J., Herndl, G. J., Hoffmann, L. J., Leach, H., Losch, M., Mills, M. M.,
1441 Neill, C., Peeken, I., Röttgers, R., Sachs, O., Sauter, E., Schmidt, M. M., Schwarz, J.,
1442 Terbrüggen, A. and Wolf-Gladrow, D.: Deep carbon export from a Southern Ocean iron-
1443 fertilized diatom bloom, *Nature*, 487, 313–319, doi:10.1038/nature11229, 2012.
- 1444 Smith, W. O. J. and Jones, R. M.: Vertical mixing, critical depths, and phytoplankton growth in
1445 the Ross Sea, *ICES J. Mar. Sci.*, 72(6), 1952–1960, 2015.
- 1446 Spackeen, J. L., Sipler, R. E., Bertrand, E. M., Xu, K., McQuaid, J. B., Walworth, N. G.,
1447 Hutchins, D. A., Allen, A. E. and Bronk, D. A.: Impact of temperature, CO₂, and iron on nutrient
1448 uptake by a late-season microbial community from the Ross Sea, Antarctica, *Aquat. Microb.
1449 Ecol.*, 82, 145–159, doi:10.3354/ame01886, 2018.
- 1450 St-Laurent, P., Yager, P. L., Sherrell, R. M., Stammerjohn, S. E. and Dinniman, M. S.: Pathways
1451 and supply of dissolved iron in the Amundsen Sea (Antarctica), *J. Geophys. Res. Ocean.*, 122(9),
1452 7135–7162, doi:10.1002/2017JC013162.Received, 2017.
- 1453 Sunda, W. G.: Trace metal interactions with marine phytoplankton, *Biol. Oceanogr.*, 6(5–6),
1454 411–442, doi:10.1080/01965581.1988.10749543, 1989.
- 1455 Sunda, W. G.: Feedback interactions between trace metal nutrients and phytoplankton in the
1456 ocean, *Front. Microbiol.*, 3, 204, doi:10.3389/fmicb.2012.00204, 2012.
- 1457 Sunda, W. G. and Huntsman, S. A.: Regulation of cellular manganese and manganese transport
1458 in the unicellular rates alga *Chlamydomonas*, *Limnol. Oceanogr.*, 30(1), 71–80,
1459 doi:10.4319/lo.1985.30.1.0071, 1985.
- 1460 Sunda, W. G. and Huntsman, S. A.: Feedback interactions between zinc and phytoplankton in
1461 seawater, *Limnol. Oceanogr.*, 37(1), 25–40, doi:10.4319/lo.1992.37.1.0025, 1992.
- 1462 Sunda, W. G. and Huntsman, S. A.: Cobalt and zinc interreplacement in marine phytoplankton:
1463 Biological and geochemical implications, *Limnol. Oceanogr.*, 40(8), 1404–1417,
1464 doi:10.4319/lo.1995.40.8.1404, 1995.
- 1465 Sunda, W. G. and Huntsman, S. A.: Antagonisms between cadmium and zinc toxicity and
1466 manganese limitation in a coastal diatom, *Limnol. Oceanogr.*, 41(3), 373–387, 1996.



- 1467 Sunda, W. G. and Huntsman, S. A.: Effect of Zn, Mn, and Fe on Cd accumulation in
1468 phytoplankton: Implications for oceanic Cd cycling, *Limnol. Oceanogr.*, 45(7), 1501–1516,
1469 2000.
- 1470 Taylor, G. T. and Sullivan, C. W.: Vitamin B12 and cobalt cycling among diatoms and bacteria
1471 in Antarctic sea ice microbial communities, *Limnol. Oceanogr.*, 53(5), 1862–1877, 2008.
- 1472 Warren, M. J., Raux, E., Schubert, H. L. and Escalante-Semerena, J. C.: The biosynthesis of
1473 adenosylcobalamin (vitamin B12), *Nat. Prod. Rep.*, 19, 390–412, doi:10.1039/B108967F, 2002.
- 1474 Westerlund, S. and Öhman, P.: Cadmium, copper, cobalt, nickel, lead, and zinc in the water
1475 column of the Weddell Sea, Antarctica, *Geochim. Cosmochim. Acta*, 55(8), 2127–2146,
1476 doi:10.1016/0016-7037(91)90092-J, 1991.
- 1477 Zhu, Z., Xu, K., Fu, F., Spackeen, J. L., Bronk, D. A. and Hutchins, D. A.: A comparative study
1478 of iron and temperature interactive effects on diatoms and *Phaeocystis antarctica* from the Ross
1479 Sea, Antarctica, *Mar. Ecol. Prog. Ser.*, 550, 39–51, doi:10.3354/meps11732, 2016.